Intrawave observations of sediment entrainment processes above sand ripples under irregular waves

R. B. O'Hara Murray,[1,2] P. D. Thorne,[2] and D. M. Hodgson[1]

Received 18 February 2010; revised 6 July 2010; accepted 3 September 2010; published 5 January 2011.

[1] Measurements of intrawave sediment entrainment processes are reported above ripples under irregular waves generated in a large-scale flume facility. The data consist of substantive observations of small-scale processes collected at high spatial and temporal resolution under irregular wave forcing, typical of coastal environments. Acoustic measurements were made of water velocities, bed forms, and suspended sediment concentration over plane and rippled beds. During each rippled bed experiment, measurements were taken over the crests of steep sided ripples, above which flow separation was considered likely to occur. Above the ripple crests, a strong intrawave variation in the near-bed suspended sediment, indicative of vortex formation and shedding, was observed to dominate wave half cycles where the orbital diameter was greater than 1.2 times the ripple wavelength λ. The irregular waves were parameterized with a significant wave height H_s and a significant orbital diameter d_{0s}. Thus, during irregular wave conditions and over steep ripples where $d_{0s}/\lambda > 1.2$, vortex shedding was deemed as the dominant sediment entrainment process. Furthermore, the percentage of wave half cycles where vortex shedding was observed, was found to scale as 26 d_{0s}/λ. These results demonstrate, for under irregular waves, the existence of a clear suspended sediment structure consistent with vortex shedding, previously observed under regular waves.

Citation: O'Hara Murray, R. B., P. D. Thorne, and D. M. Hodgson (2011), Intrawave observations of sediment entrainment processes above sand ripples under irregular waves, *J. Geophys. Res.*, *116*, C01001, doi:10.1029/2010JC006216.

1. Introduction

[2] In oscillatory flow and above steep, two-dimensional (2D) ripples, the boundary layer between the flow and the bed can separate in the lee of the ripple, thus forming a vortex which at flow reversal is ejected into higher parts of the flow. The near-bed hydrodynamics and momentum transfer is dominated by vortex formation and shedding and the effect that this process has on near-bed sediment suspensions is profound. Sediment can be trapped in the shed vortex, which is advected both horizontally and vertically [*Bijker et al.*, 1976; *Hansen et al.*, 1994], and is released as the vortex propagates above the bed and dissipates as turbulence becomes dominant. Under vortex shedding conditions maximum sediment pickup occurs as the vortex is advected over the ripple crest around the instant of flow reversal [*Nakato et al.*, 1977; *Sleath and Wallbridge*, 2002]. In contrast, over a flat bed where vortex shedding does not occur, maximum sediment pickup occurs at times of peak shear stress at the bed, closely preceding peak free-stream velocity [*Davies and Thorne*, 2008]. *Davies and Villaret* [1999] interpreted the vortex shedding process above ripples in terms of a convective stress close to the bed, described by a strongly time varying convective eddy viscosity with peaks at flow reversal. The time dependence of such a convective eddy viscosity has also been examined with a cloud-in-cell discrete vortex model, above a ripple bed, and peaks were observed to occur at flow reversal [*Malarkey and Davies*, 2004]. Thus, these different entrainment processes impact upon the respective mixing mechanisms above flat and rippled beds: Coherent convective processes dominate close to rippled beds under vortex shedding conditions, whereas turbulent diffusion dominates above flat beds [*Nielsen*, 1992; *Thorne et al.*, 2009a]. More recently, these convective and diffusive mixing processes have been related to the form of the sediment diffusivity profile [*Thorne et al.*, 2009a].

[3] It is becoming increasingly well-established that the coherent and repeatable phenomenon of vortex shedding above ripples can entrain sediment to considerably greater heights than above a flat bed. This is true both in a time averaged sense [e.g., *Thorne et al.*, 2002] and at certain phases during the wave cycle [e.g., *Bijker et al.*, 1976; *Nakato et al.*, 1977; *Block et al.*, 1994; *Davies and Thorne*, 2005; *van der Werf et al.*, 2007]. Under symmetrical waves the vortex shedding process occurs twice every wave cycle: On the onshore and offshore sides of the ripple crest, during the onshore and offshore phases of the wave cycle, respectively. The ejection of sediment laden vortices above the ripple crest occurs at flow reversal and this leads, for

[1]School of Environmental Sciences, University of Liverpool, Liverpool, UK.
[2]National Oceanography Centre, Liverpool, UK.

0148-0227/11/2010JC006216

example, to the vortex generated during the onshore wave half cycle being advected in the offshore direction. Thus, under asymmetric waves where the onshore orbital velocities are largest, an offshore pumping of sediment can occur [*Bijker et al.*, 1976; *Davies and Thorne*, 2008].

[4] The process of vortex formation and shedding is inherently linked to the bed forms present under such conditions, namely vortex ripples, over which flow separation can occur. Under quiescent wave forcing conditions the bed forms present are often those of relicts remaining from times of stronger wave activity [*Nielsen*, 1992], otherwise the bed is nominally plane. During these conditions, which can be described as lower-stage plane bed, there is little in the way of suspended sediment pickup as the bed shear stress is low and the relict bed forms are nonactive. Under surface waves of low steepness, long-crested 2D ripples start to emerge on the bed. As the surface wave steepness increases, the ripple steepness increases and boundary layer separation is initiated. During these conditions vortex ripples become active and begin to shed vortices. Thus, vortex ripples spread over the bed and the process of vortex formation and shedding can dominate the suspended sediment dynamics. As the steepness of the surface waves increases further, the bed forms reduce in steepness and tend toward a (transitional) three-dimensional (3D) morphology where the crests first become sinuous and broken in form before becoming washed out. Eventually, as surface wave steepness continues to increase toward storm conditions, the bed becomes an upper-stage plane bed with sheet flow dominant.

[5] Ripples with wavelengths that scale with the wave orbital diameter, termed orbital ripples [*Clifton*, 1976; *Clifton and Dingler*, 1984], are predominant in laboratory experiments and are steep sided with ripple height to wavelength ratios (steepness) greater than 0.1. While orbital ripples can be found in the field, anorbital ripples, with wavelengths roughly proportional to the bed sediment grain size, are much more common [*Wiberg and Harris*, 1994]. Anorbital ripples occur when the orbital diameter is larger than the ripple wavelength. Thus, anorbital ripples can be referred to as decaying ripples, present at times of transition between orbital ripples and upper-stage plane bed [*Allen*, 1997]. Suborbital ripples are a transitional type and occur when the orbital diameter is between that of orbital and anorbital ripples.

[6] Some of the earliest observations of vortex entrainment of sediment above ripples were made by *Bagnold* [1946] in an oscillating water tank. *Bijker et al.* [1976] inferred the process of vortex shedding from observations of suspended sand transport opposite to the direction of wave propagation as well as making photographic observations of the vortex shedding and sediment entrainment process. Some of the earliest intrawave measurements of suspended sediment concentration (SSC) were made by *Nakato et al.* [1977] in regular oscillatory flow generated in a water tunnel. *Nakato et al.* [1977] observed two dominant peaks in the SSC during the wave cycle and contributed these to vortex ejection during each wave half cycle. Vortex shedding has also been directly observed in the laboratory under regular [*Tunstall and Inman*, 1975] and irregular [*Villard and Osborne*, 2002] free surface waves and its existence has been inferred in the field [*Ardhuin et al.*, 2002]. Observations of SSC have been made under waves and over ripples on a macrotidal beach where a weak current was present using an Acoustic Backscatter System (ABS) [*Osborne and Vincent*, 1996], although evidence of vortex generation was only found during the onshore phase of the wave cycles. More recently, the SSC profile on an intrawave time scale under regular oscillatory flow has been measured using ABS [*Thorne et al.*, 2003; *Davies and Thorne*, 2005; *van der Werf et al.*, 2007]. A coherent phenomenon consistent with the entrainment of sediment in a lee-wake vortex shed at flow reversal was identified, thus confirming the existence of vortex entrainment processes at large scale under regular oscillatory flow. One recent development was that of *Nichols and Foster* [2007] who made observations of the near-bed velocity field, above an asymmetrical ripple under irregular waves in a large wave flume, using a Particle Image Velocimetry (PIV) system and found that the ejection of a vortex was a function of the flow acceleration.

[7] In laboratory experiments, regular waves are often used for simplicity, however irregular waves simulate nature more closely [*Soulsby*, 1997], containing a broad spectrum of wave heights and periods. The near-bed velocity field under regular waves provides a repeatable orbital excursion that is conducive to both the formation of wave ripples and the subsequent formation of lee-wake vortices in each wave half cycle. In contrast to regular waves, the horizontal velocity field under irregular waves has a distribution of velocity amplitudes, oscillation periods, and thus orbital excursion diameters, which govern the formation of ripples and the suspension of sediment. Thus, vortex formation and shedding will not necessarily occur during each wave half cycle under irregular waves. It is questionable therefore, whether the intrawave signatures present in the suspended sediment dynamics of vortex formation and shedding are dominant under irregular waves, as is the case under regular oscillatory flow [e.g., *Davies and Thorne*, 2005; *van der Werf et al.*, 2007]. Furthermore, it is at present unknown in an irregular wave sequence, under which wave half cycle vortex formation occurs. Refining our understanding of this has significant implications as many models simply characterize the flow with average parameters such as the significant wave height (H_s). It is therefore useful to quantify the fraction of waves where vortex shedding is expected to occur under different hydrodynamic regimes, described by H_s for example.

[8] The Deltaflume of Deltares, Delft Hydraulics, Netherlands, is a large flume facility ideal for the study of sediment transport processes at near field-scales. In 2001, a comprehensive dataset of measurements covering the sediment transport triad of wave forcing, bed forms, and suspended sediment [*Thorne and Hanes*, 2002] was collected, under irregular waves. These data have been reported previously in studies focusing on bed forms [*Williams et al.*, 2004; *Williams and Bell*, 2006]. In the present study, the bed forms are re-examined and the intrawave structure of the suspended sediments is studied for the first time. The underlying questions this present study addresses are: (1) Whether vortex formation and shedding is a dominant mechanism of sediment entrainment under irregular waves; (2) under what proportion of wave half cycles this mechanism occurs; and (3) whether these occurrences can be parameterized by the ratio of orbital diameter to ripple

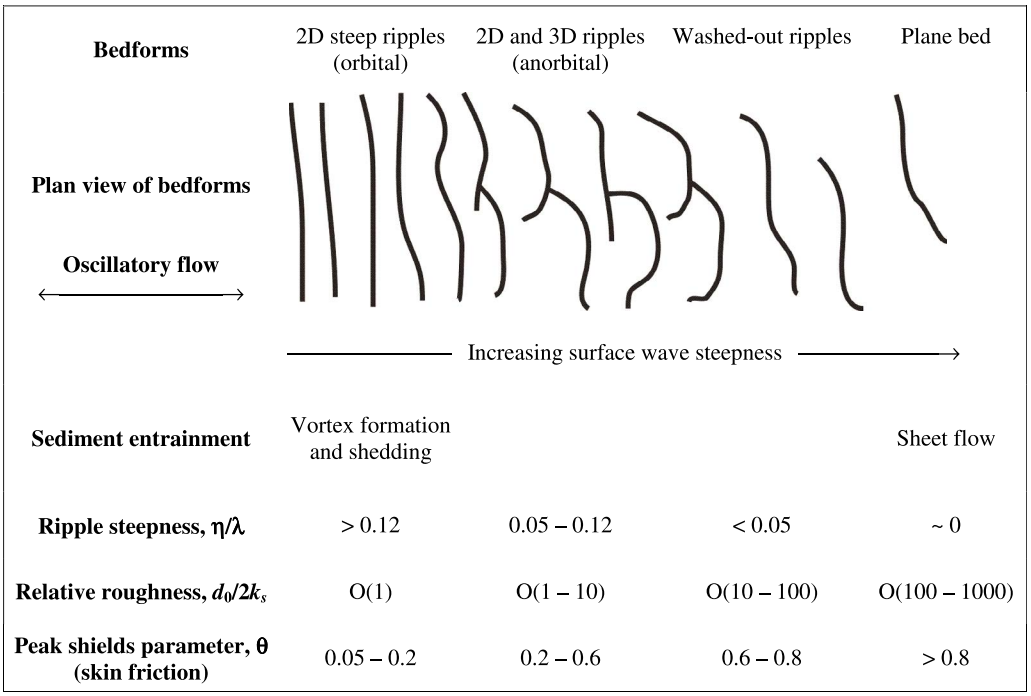

Figure 1. Schematic of bed form characteristics related to hydrodynamic and bed form parameterizations (based on work by *Davies and Thorne* [2008] and *Thorne et al.* [2009a]). For relative roughness, O indicates "of the order."

wavelength as suggested by *Malarkey and Davies* [2002]. Finally, irregular wave forcing is often parameterized by the significant wave height which is in turn commonly used within models. Hence, in the present study the relationship between the significant wave height, the ripple dimensions, and the occurrence of vortex shedding is investigated because of the direct relevance this has with existing numerical modeling frameworks.

2. Models and Prediction of Vortex Shedding

[9] *Davies and Thorne* [2008] presented a simple modeling framework for oscillatory flow above erodible sandy beds. Figure 1 shows a schematic of common bed form regimes under regular oscillatory flow, from the vortex shedding regime to the upper-stage plane bed, under increasing surface wave steepness. Beneath (regular) waves, the orbital excursion diameter of each wave half cycle, d_0, scales with the surface wave steepness. Key to parameterizing bed form regimes is the Shields parameter, a dimensionless measure of the balance between disturbing (shear stress) and stabilizing forces on individual surface sediment particles. Figure 1 shows the skin friction Shields parameter, θ, increasing with the surface wave steepness. Another parameterization is the relative roughness, $d_0/2k_s$, where k_s is the equivalent roughness which describes the influence the bed has on the flow. Above lower-stage plane beds, the dominate contribution to the roughness is the Nikuradse grain roughness due to skin friction, typically given by [*Soulsby*, 1997]

$$k_s = 2.5D_{50}. \tag{1}$$

Based on this equivalent grain roughness, the grain roughness Shields parameter, $\theta_{2.5}$, can be defined as [e.g., *Nielsen*, 1992]

$$\theta_{2.5} = \frac{f_{2.5}U_0^2}{2(s-1)gD_{50}}, \tag{2}$$

where s is the ratio of sediment density to water density (s = 2.65 for quartz sand), D_{50} is the median grain diameter of the bed sediment, g is the acceleration due to gravity, U_0 is the wave orbital amplitude, and $f_{2.5}$ is the grain roughness wave friction factor (skin friction) based on equation (1). One expression for $f_{2.5}$ is that developed by *Soulsby* [1997] for rough turbulent flow which, with equation (1) substituted in, is given by

$$f_{2.5} = 0.237(d_0/5D_{50})^{-0.52}. \tag{3}$$

When bed forms are present, the dominant contribution to the roughness is due to form drag [*van Rijn*, 2007] and k_s is often expressed in terms of the ripple dimensions. One commonly used form for k_s above a rippled bed is [*Grant and Madsen*, 1982; *Nielsen*, 1992; *Styles and Glenn*, 2002; *Davies and Thorne*, 2008]

$$k_s = \alpha\eta(\eta/\lambda), \tag{4}$$

where η and λ are the height and wavelength, respectively, of the ripples present on the bed. There are conflicting reports as to the precise value of α. For example, *Grant and Madsen* [1982] proposed α = 27.7 whereas *Nielsen* [1992] proposed α = 8. There can also be roughness associated with a moving sand layer, during sheet flow conditions; for

example [*Grant and Madsen*, 1982; *Nielsen*, 1992], such as [*Nielsen*, 1992]

$$k_s = 170 D_{50} \sqrt{\theta_{2.5} - 0.05}. \quad (5)$$

Nielsen [1992] proposed that above ripples both the form drag due to the ripples and the moving sand layer contribute toward the total equivalent roughness, such that

$$k_s = 8\eta \frac{\eta}{\lambda} + 170 D_{50} \sqrt{\theta_{2.5} - 0.05}. \quad (6)$$

2.1. Vortex Shedding Criteria

[10] The ripples above which vortex formation and shedding occur are termed vortex ripples and are typical during the '2D steep ripple' regime defined in Figure 1. Vortex shedding occurs only when the ripples are sufficiently steep for the boundary layer to separate on the lee of the ripple crests [*Sleath*, 1984]. Hence, the steepness of the ripple is one control over whether vortex formation and shedding occur and is used in the expression for k_s above rippled beds (equation (4)). It is widely assumed that vortex shedding only starts when $\eta/\lambda \gtrsim 0.1$ [*Davies and Thorne*, 2005]. *Allen* [1979] suggested that $\eta/\lambda \approx 0.13$ marks the transition from rolling-grain to vortex ripples and *Malarkey and Davies* [2004] considered $0.13 \leq \eta/\lambda \leq 0.2$ to define an approximate vortex shedding regime. Likewise, *Davies and Villaret* [2002] considered the bed to be 'dynamically plane', where no vortex shedding processes occur, when $\eta/\lambda < 0.12$. Thus, the η/λ values in Figure 1 indicate whether flow separation is likely to occur in each regime.

[11] As indicated in Figure 1, $d_0/2k_s$ increases with the evolving bed under progressively increasing wave steepness. In the vortex ripple regime, where $d_0/2k_s \sim O(1)$, k_s is related to the ripple dimensions by equation (4). Taking the ripple steepness as $\eta/\lambda = 0.12$ and $\alpha = 8$ [*Nielsen*, 1992], k_s can be related the ripple height, $k_s = 0.96\eta$, or the ripple wavelength, $k_s = 0.1252\lambda$, and in the vortex shedding regime the relative roughness is given by

$$d_0/2k_s \approx 4.34 d_0/\lambda. \quad (7)$$

Malarkey and Davies [2002] used the parameter d_0/λ to define a secondary vortex shedding criterion, $1 \leq d_0/\lambda \leq 4$, which roughly equates to $4.3 \leq d_0/2k_s \leq 17.4$ using equation (7). This criteria, $1 \leq d_0/\lambda \leq 4$, has significant implications for sediment entrainment and transport. Beneath regular waves, where d_0/λ is relatively constant, this is not such an issue, but beneath irregular waves it implies that vortex shedding will occur intermittently due to the distribution of orbital diameters. When d_0/λ is between 1 and 4, vortex shedding is expected to dominate the entrainment of sediment. The nonseparating flow limit, $d_0/\lambda = 1$, is where it is unlikely for the flow to be strong enough for boundary layer separation to occur. The upper limit, $d_0/\lambda > 4$, defines the point where the organized flow structure of vortex formation and shedding starts to give way to more homogenous turbulence where peaks in the sediment pickup occur at phases that are more in line with flat bed (sheet flow) behavior [*Malarkey and Davies*, 2002]. The observations of *Nichols and Foster* [2007] using PIV confirmed both intermittent vortex shedding under irregular waves and also its dependence on the flow velocity (related to the orbital excursion). The dependence of the parameter d_0/λ on the ripple wavelength has strong implications in the natural environment where there is likely to be a distribution of ripple wavelengths present on the bed. The dependence of vortex shedding on d_0/λ has been examined theoretically with cloud-in-cell and discrete vortex models and compared with laboratory measurements of the water particles in two-dimensions [*Malarkey and Davies*, 2002], but not to our knowledge under field-scale irregular waves, or through observations of the suspended sediments and fluid flow.

2.2. Suspended Sediment Concentrations

[12] One method of predicting the sediment concentration under oscillatory flow is to separate the magnitude and distribution of SSC above the bed. For example, the time averaged profile of SSC above ripples and under waves, $C(z)$, is often expressed in the form

$$C(z) = C_0 \exp(-z/L), \quad (8)$$

where z is the height above the bed and L is the vertical decay length scale. The reference concentration, typically taken at the bed level, is a measure of the concentration magnitude and is commonly expressed theoretically in terms of the grain roughness Shields parameter ($\theta_{2.5}$) given by equation (2). Above ripples, *Nielsen* [1986] modified $\theta_{2.5}$ to account for flow enhancement near the ripple crest:

$$\theta_r = \frac{\theta_{2.5}}{(1 - \pi\eta/\lambda)^2}, \quad (9)$$

where λ and η are the wavelength and height of the ripples, respectively. *Nielsen* [1986] found a cubic dependence of the mass reference concentration, C_0, taken over the ripple crest (at crest level) on θ_r:

$$C_0 = 0.005 \rho_s \theta_r^3, \quad (10)$$

where ρ_s is the sediment density. Equation (10) was confirmed by *Thorne et al.* [2002] under large-scale regular waves although the empirical coefficient, 0.005 in equation (10), was found to be 0.0022 ± 0.0005, close to a factor of two smaller.

[13] Reference concentrations based on the Shields parameter, for example equation (10), are time averages, often over many wave cycles, that is, $C_0 = \overline{c_0(t)}$ where $c_0(t)$ is the instantaneous reference concentration as a function of time (t) and the over bar indicates a time average. Similarly, the grain roughness Shields parameter defined as $\theta_{2.5}$ in equation (2) is based on the orbital velocity amplitude, U_0. It follows that the instantaneous, time varying, reference concentration, $c_0(t)$, cannot be straightforwardly expressed in terms of $\theta_{2.5}$ and θ_r defined here. From a modeling point of view, *Davies et al.* [1997] discussed the difficulties associated with applying the reference concentration approach in time dependant sediment suspension problems. They commented that one way to overcome these difficulties is with the use of a time varying sediment pickup function based on the SSC gradient near the bed. Nevertheless, it is established that variations in sediment entrain-

ment through the wave cycle lead to instantaneous variations in $c_0(t)$, and therefore that sediment pickup and $c_0(t)$ are intrinsically linked.

[14] *Nielsen* [1992] suggested empirical equations for the decay length scale of the SSC profile given by equation (8):

$$L = \begin{cases} 0.075\dfrac{U_0}{w_s}\eta & \dfrac{U_0}{w_s} < 18 \\ 1.4\eta & \dfrac{U_0}{w_s} \geq 18. \end{cases} \quad (11)$$

The settling velocity of the suspended sediment, w_s, can be calculated from knowledge of the median grain size of the suspended sediment, D_{s50}, using the formula of *Soulsby* [1997]

$$w_s = \frac{\upsilon}{D_{s50}}\left[\sqrt{10.36^2 + 1.049D_*^3} - 10.36\right], \quad (12)$$

where υ is the kinematic viscosity of water and D_* is a dimensionless grain size given by

$$D_* = \left[\frac{g(s-1)}{\upsilon^2}\right]^{1/3} D_{s50}. \quad (13)$$

Under fixed wave forcing conditions (e.g., U_0 = 1 m/s), U_0/w_s is <18 typically when coarse sediments (i.e. $w_s > 18^{-1}$ m/s, $D_{s50} \gtrsim 370$ μm) are in suspension. In this case, L varies with U_0/w_s and the ripple height (η). When $U_0/w_s > 18$, that is for finer sediment (explicitly $w_s \leq 18^{-1}$ m/s, $D_{s50} \lesssim 370$ μm), L is only dependant on η, and $C(z)$ decays at the same rate under different wave forcing conditions as long as the ripples have the same height. When $U_0/w_s < 18$, that is, when coarse sediments are in suspension, equation (11) is dependent on the sediment settling velocity. This is likely to be a source of uncertainty in the prediction of L where a broad sediment size distribution is present. In these cases the settling velocity distribution should be considered. It is worth noting that there has been some work on the suspensions of graded sediment [e.g., *Nielsen*, 1983; *Nielsen*, 1992; *Tomkins et al.*, 2003].

3. Experimental Instrumentation and Methodology

[15] Irregular waves with a Joint North Sea Wave Project (JONSWAP) spectrum [*Carter*, 1982] were generated for a number of significant wave heights in the Deltares Delft Hydraulics Deltaflume. This large scale flume (230 m long, 5 m wide, and 7 m deep) enables a variety of sediment transport processes to be monitored at field scale.

[16] Experiments were conducted first over a fine-medium-grained sand bed and then over an upper-medium-grained sand bed. Using laser granulometry, the two sediment beds were found to have grain size distributions lognormal in form, with the fine-medium-grained bed having D_{10} = 161 μm, D_{50} = 258 μm, and D_{90} = 408 μm and the upper-medium-grained bed having D_{10} = 243 μm, D_{50} = 375 μm, and D_{90} = 577 μm. In each case, a 0.7 m deep sediment bed was laid down in the center of the flume in a 30 m long region spanning the width of the flume. A series of experiments were performed over each sand bed. For both the fine-medium-grained and upper-medium-grained experiment sets, the sand bed was initially a horizontal plane bed (P. S. Bell and J. J. Williams, Comprehensive measurements of sediment resuspension processes by waves at full-scale, Internal Document 143, Proudman Oceanographic Laboratory, Liverpool, U.K.) and was not flattened between experiments such that each experiment inherited the bed morphology formed during the previous experiment. Each experiment differed only by the significant wave height H_s of the surface wave forcing, such that, over the course of the experiments, H_s varied between 0.2 and 1.9 m. In total, 16 experiments were conducted over the fine-medium-grained sand bed, referred to here as F01, F02, …, F16, and 17 experiments were conducted over the upper-medium-grained sand bed, referred to here as M01, M02, …, M17. The peak spectral period was held at a constant 6.1 s during all the experiments.

[17] Figure 2 is a schematic of the instruments deployed on a frame aligned to one side of the flume on the sandy bed. In this study, acoustic data from two Nortek Acoustic Doppler Velocimeters (ADV-1 and ADV-2), an Acoustic Ripple Profiler (ARP), a Sector Scanning Sonar (SSS), and an Acoustic Backscatter System (ABS) were examined to study water velocities, bed form cross-sections, plan-form bed form features, and suspended sediments, respectively. A pump sampling system [*Bosman et al.*, 1987] was mounted on the instrument frame and samples of the suspended sediment laden water were taken during a number of experiments and were used here to provide time-averaged suspended particle size and concentration. The horizontal (along-shore) and vertical positioning of the instruments, relative to the side of the instrument frame closest to the wall of the Deltaflume and the surface of the undisturbed sandy bed, respectively, are indicated in Figure 2. During the course of the experiments the local level of the sand bed varied due to ripple formation and to the feet of the instrument frame settling into the sand. Thus, the vertical distances between the instruments and the sandy bed varied over the experimental period. The SSS operated at 1.2 MHz mechanically scanning through 400 angular steps during each revolution taking approximately 60 s [*Williams et al.*, 2004] and was positioned at the onshore end of the instrument frame. The ARP operated at 2 MHz scanning a 4 m transect of the bed approximately every 63 s at centimeter horizontal resolution and subcentimeter vertical resolution providing a 2D profile of the bed, and how it changed with time. The 16 Hz time-series obtained from the ADVs consisted of 3 orthogonal components of flow: Horizontal along-flume (cross-shore); horizontal across-flume (along-shore); and vertical. ADV-1 and ADV-2 were mounted on the frame such that their measuring volumes were 0.57 and 0.145 m above the base of the instrument frame, respectively, measuring the free-stream and near-bed water velocities, respectively. The ABS comprised 3 transducers aligned perpendicular to the flow (along-shore), operating at 1, 2, and 4 MHz, and these monitored the SSC above the bed at 1 cm vertical resolution. The ABS collected backscatter profiles at 128 Hz at each frequency, which were each subsequently block averaged in order to improve the statistical reliability of the results to produce backscatter profiles at 4 Hz. The pumped samples were dry weighed yielding time averaged concentration measurements at five heights above the bed. A multiplication factor of 1.4 was

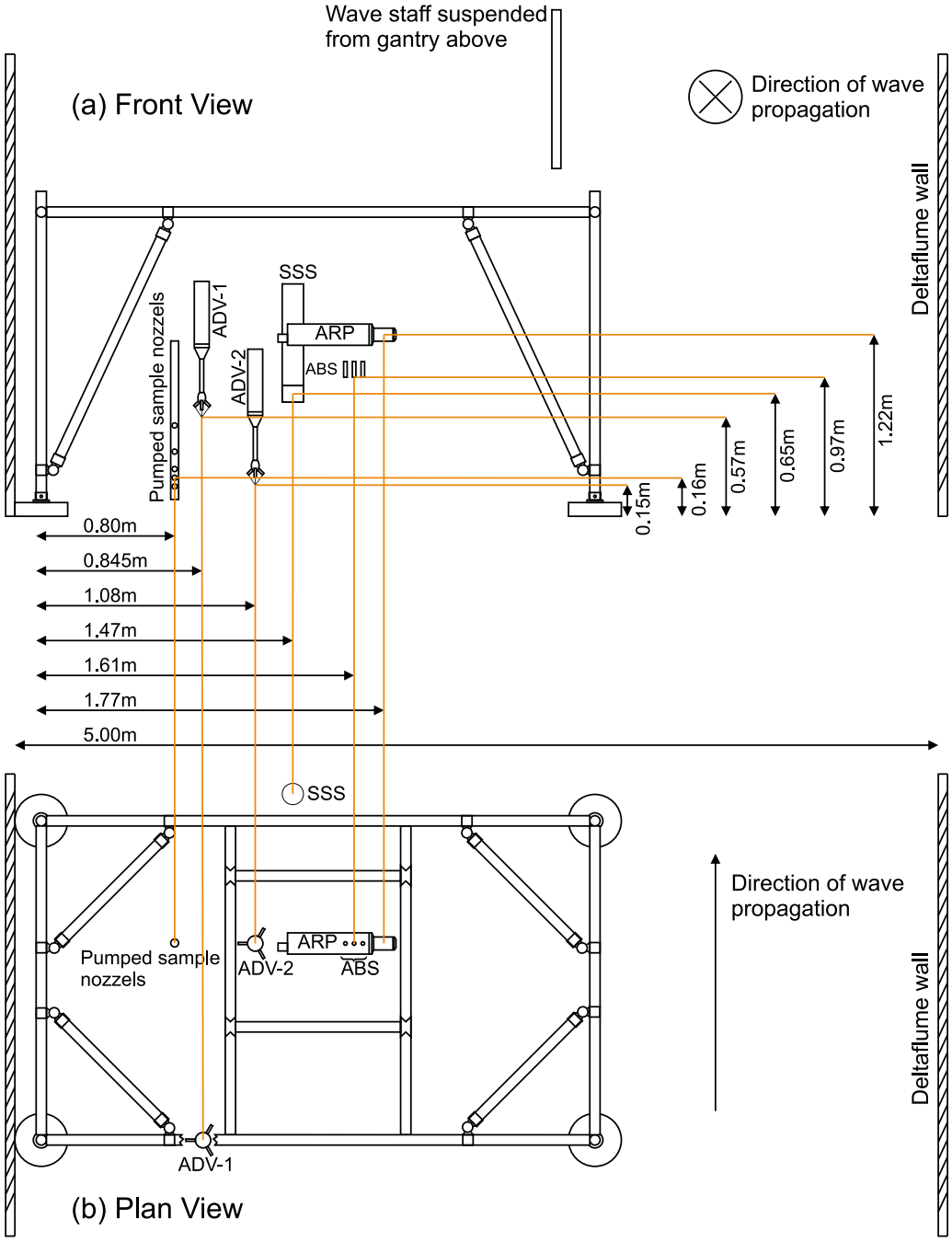

Figure 2. Schematic of the instrument frame deployed in the Deltaflume with the locations of the Acoustic Ripple Profiler (ARP), Acoustic Backscatter System (ABS), Acoustic Doppler Velocimeters (ADV-1 and ADV-2), Sector Scanning Sonar (SSS), and pump sampling nozzles indicated.

applied to the pumped sampled sediment concentrations on the basis of the findings of *Bosman et al.* [1987]. Subsequently, the dried pumped samples were analyzed using laser diffraction to obtain the distribution of grain sizes. The ARP, ABS, and ADV-2 were collocated on an along-shore line (perpendicular to the flow) ensuring that they were approximately at the same location on a 2D ripple cross-section. Finally, the elevation of the water surface was monitored by a wave staff mounted on a gantry above the flume. Further details of the Deltaflume, the 2001 experimental setup, and the instruments deployed were presented by *Williams et al.* [2003, 2004, 2005] and *Williams and Bell* [2006].

[18] In the present study, data from four Deltaflume experiments are examined. The first, F08, was selected on the grounds that vortex ripples were not present and the bed approximated to an upper-stage plane bed above which no rippled bed sediment dynamics occurred. During experiments M04, M05 and M06, steep-sided ripples, the dimensions of which conformed to descriptions of vortex ripples, were present. During these three experiments the ABS was above a ripple crest, and these measurement

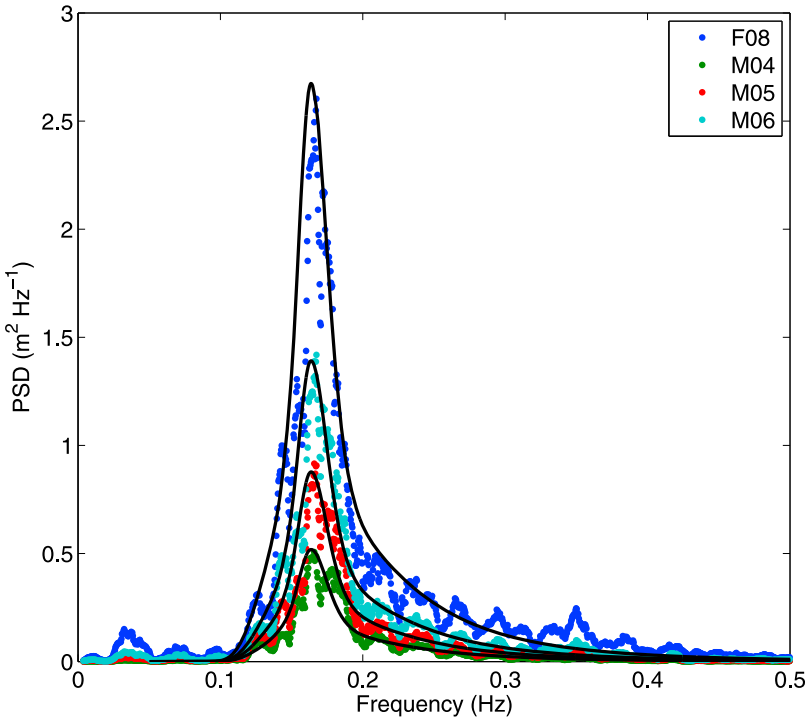

Figure 3. The power spectral density (PSD) of the surface elevation recoded by the wave staff during four Deltaflume experiments with a 21 point running average applied and the theoretical JONSWAP spectra (black lines) with measured H_s and T_p as inputs and a peak enhancement factor of $\gamma = 3.3$.

periods are referred to in the present study as 'measurement bursts'. To summarize, data from F08 and M04–M06 enabled flat bed and rippled bed sediment dynamics, respectively, to be studied under irregular waves. The profiles of SSC were phase locked to the ADV velocities. Thus, working in the phase domain, ensemble averages over many wave cycles were computed, enabling the underlying intrawave structure of the SSC above plane and rippled beds and under irregular waves to be studied. Whether this intrawave structure, beneath irregular waves, displays the same features in the rippled bed cases to that below regular waves [e.g., *Davies and Thorne*, 2005] is investigated in the present study.

4. Data Analysis and Results

4.1. Irregular Wave Forcing

[19] The irregular surface waves were generated conforming to JONSWAP spectra (P. S. Bell and J. J. Williams, Comprehensive measurements of sediment resuspension processes by waves at full-scale, Internal Document 143, Proudman Oceanographic Laboratory, Liverpool, U.K.) and the elevation was measured at 25 Hz by wave staffs suspended above the flume. The significant wave height H_s was calculated for each experiment as [e.g., *Soulsby*, 1997; *Wiberg and Sherwood*, 2008]

$$H_s = 4\sqrt{m_0}, \tag{14}$$

where m_0 is the variance of the water surface elevation. The peak spectral period T_p for each experiment was taken as the inverse of the frequency at which the power spectral density of the water surface elevations peaked. Table 1 lists the calculated values of H_s and T_p for each experiment. The dispersion equation was solved using average water depths h, obtained from a pressure sensor present in the Deltaflume, and T_p. Table 1 lists the water depths and resulting wave numbers, k, together with predictions of the significant velocity amplitude, U_{0s}, and the orbital excursion diameter, d_{0s}, based on linear wave theory:

$$U_{0s} = \frac{\pi H_s}{T_p \sinh(kh)} \tag{15}$$

$$d_{0s} = U_{0s} T_p / \pi. \tag{16}$$

These U_{0s} and d_{0s} values were used in place of U_0 and d_0 in equations (2) and (3) to calculate $\theta_{2.5}$ and $f_{2.5}$ for each experiment, and the results are included in Table 1. The spectra of the water surface elevation were examined and compared with theoretical JONSWAP spectra [*Carter*, 1982; *Podgorski et al.*, 2000] based on the observed values of H_s and T_p. Figure 3 presents the theoretical and observed wave spectra for each experiment, and shows that the theoretical spectra compare well with the data, in both amplitude and width.

4.2. Bed Forms

[20] The bed forms were observed using an ARP and a SSS. The ARP time series were examined and, in the case of the rippled bed experiment, temporal regions where the ripples were in a steady state and the ARP was consistently over a ripple crest were identified. These temporal regions

Table 1. Temporally Averaged Experimental Parameters for the Deltaflume Experiments

	H_s (m)	T_p (s)	h (m)	k (m^{-1})	U_{0s} (m/s)	d_{0s} (m)	$f_{2.5}$	$\theta_{2.5}$	d_{0s}/D_{50}
F08	1.45	6.11	3.99	0.18	0.98	1.91	0.0053	0.61	7388
M04	0.64	6.11	4.01	0.18	0.43	0.84	0.0099	0.15	2230
M05	0.83	6.11	4.01	0.18	0.56	1.09	0.0087	0.22	2904
M06	1.05	6.11	3.97	0.18	0.71	1.38	0.0077	0.32	3682

defined the burst for each rippled bed experiment during which the data were examined. Similarly, for the plane bed experiment (F08) a burst was chosen on the grounds that the bed was in a steady state throughout. Figure 4 shows the temporal variation in these 2D bed profiles during the bursts, which were low-pass filtered with a Gaussian filtering window to remove high frequency spatial fluctuations. Figure 4a, F08, for the fine-medium-grained bed shows the remnants of a rippled bed which was washed out to form a long wavelength bed form, similar to those observed by *Hanes et al.* [2001]. This washed out bed approximates, for the purposes here, to an upper-stage plane bed above which no rippled bed sediment dynamics were expected to occur. Equation (5) was used to calculate the equivalent roughness due to a moving sand layer, and this yielded a relative roughness of $d_{0s}/2k_s = 28.97$. This $d_{0s}/2k_s$ value and the Shields parameter for F08 listed in Table 1 place F08 within the washed-out ripples regime in Figure 1. Figures 4b–4d show that during the upper-medium-grained experiments rippled beds were formed. A turning point analysis was performed to extract the spatial distribution of ripple wavelengths, heights, and steepness for each profile. The wavelength of a ripple was taken as the distance between two troughs surrounding a crest, the height of this ripple was taken as the mean crest to trough height difference on either side of the ripple crest and the steepness was taken as the height to wavelength ratio. Table 2 lists the spatial and temporal mean ripple wavelengths (λ), heights (η), and steepness (η/λ) and their associated standard deviations (σ) for the rippled bed experiments. The temporal mean average

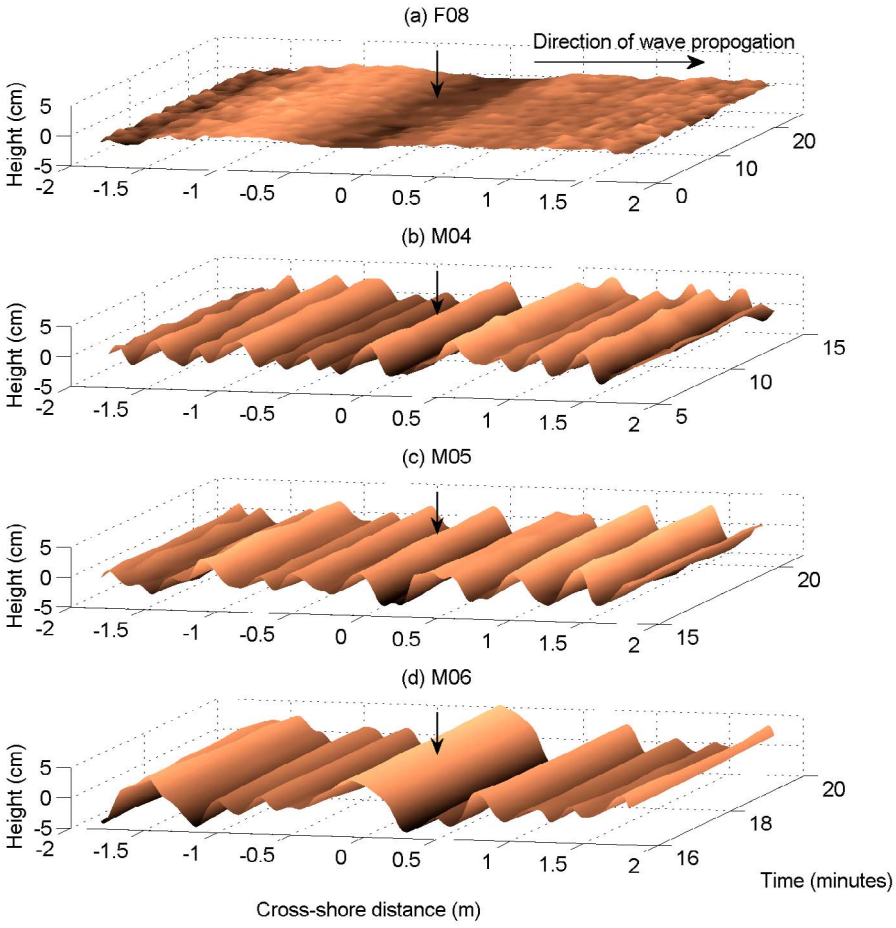

Figure 4. Bed profiles obtained from the ARP during (a) plane bed and (b–d) rippled bed Deltaflume experiments. The measurement bursts considered during the rippled bed experiments were chosen on the grounds that a crest of a ripple was below the ABS situated above the origin of the horizontal (cross-shore) axis, indicated by the arrows Figures 4a–4d.

Table 2. Mean Cross-Sectional Dimensions of the Ripples Along the Whole ARP Transect (λ, η, and η/λ) and Those Individual Ripples in Line With the ABS (λ_0, η_0, and λ_0/η_0) Along With Their Standard Deviations (σ) for Each of the Rippled Bed Bursts Considered

	Spatially and Temporally Averaged Ripple Dimensions						Temporally Averaged Dimensions of Ripple Below ABS					
	λ (m)	σ (m)	η (m)	σ (m)	η/λ	σ	λ_0 (m)	σ (m)	η_0 (m)	σ (m)	η_0/λ_0	σ
M04	0.25	0.02	0.0254	0.0018	0.09	0.01	0.33	0.01	0.0468	0.0032	0.14	0.01
M05	0.23	0.01	0.0256	0.0015	0.10	0.00	0.34	0.01	0.0462	0.0025	0.13	0.01
M06	0.33	0.02	0.0331	0.0029	0.09	0.01	0.73	0.01	0.0770	0.0080	0.11	0.01

dimensions of the ripple directly below the ARP transducer during each experiment (λ_0, η_0, and η_0/λ_0) were also calculated and the results are shown in Table 2.

[21] Figure 5 shows the temporal mean cross-section 0.6 m either side (on a cross-shore line) of the ARP, ABS, and ADV-2 for each of the four experiments. Figure 5 clearly shows that during the rippled bed bursts the acoustic devices were approximately above a ripple crest. The spatial and temporal average ripple steepness in the rippled bed cases (η/λ, Table 2) are close to 0.1, above which vortex shedding starts to occur [*Davies and Thorne*, 2005]. The steepness of the ripples directly below the acoustic instrumentation (η_0/λ_0, Table 2) were above this threshold, suggesting that it was likely that vortex shedding occurred below the ABS transducers.

[22] In addition to the ARP cross-sections, the SSS data were examined in order to reveal the plan-form geometry of the rippled beds. The SSS data were rectified from polar coordinates to square grid and a slant range correction was applied (P. S. Bell and J. J. Williams, Comprehensive measurements of sediment resuspension processes by waves at full-scale, Internal Document 143, Proudman Oceanographic Laboratory, Liverpool, U.K.). Figure 6 shows the SSS results in the form of 2D 5 × 5 m images of the bed produced just prior to the measurement bursts considered here. The temporally and spatially average ripple wavelengths obtained from the ARP (Table 2) during M04–M06 are indicated in Figures 6b–6d and show the ripple crest lengths to be typically longer than their wavelengths. However, the ripple crests are sinuous, especially during M05 and M06. The grain roughness Shields parameters

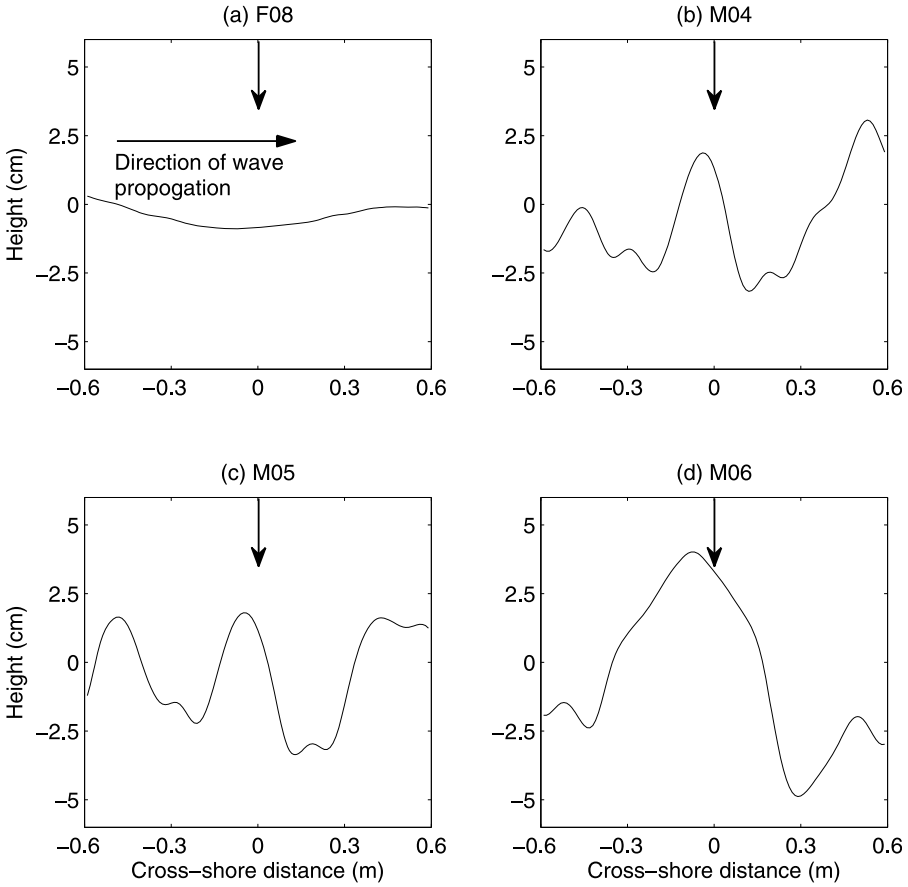

Figure 5. Time-mean of the ARP bed profiles under the ABS during (a) plane bed and (b–d) rippled bed experiments when the ABS was approximately above a ripple crest. The ARP, ABS, and ADV-2 were nominally positioned above the origin of the horizontal cross-shore axis, indicated by the arrows in Figures 5a–5d.

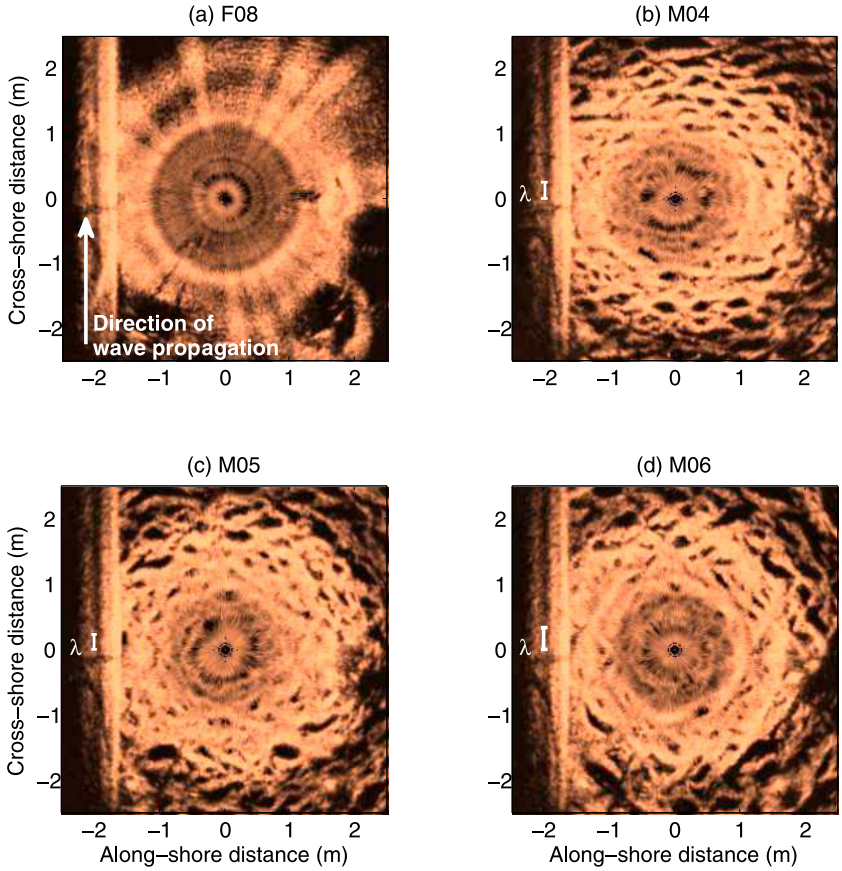

Figure 6. Sector Scanning Sonar (SSS) results from (a) plane bed and (b–d) rippled bed Deltaflume experiments. In the case of the rippled bed experiments (Figures 6b–6d) the typical ripple wavelengths, λ, determined by analysis of the ARP data are indicated.

($\theta_{2.5}$) for M04, M05, and M06 listed in Table 1 suggest (using the parameterizations in Figure 1) the bed forms present were 2D during M04 and M05 and dominantly 2D with 3D ripples emerging during M06. Such a classification is in agreement with the results from the ARP (Figures 4 and 5) and the SSS (Figure 6). Using the dimensions of the ripples below the ABS (η_0 and η_0/λ_0, Table 2) and equation (6), $d_{0s}/2k_s$ was calculated to be 5.75, 7.30, and 6.85 during experiments M04, M05, and M06, respectively. These values are broadly in agreement with the dominantly 2D classification using the $\theta_{2.5}$ values, although suggestive that both M05 and M06 should have 3D ripples emerging, which broadly agrees with the SSS images (Figure 6). Using instead the dimensions of the spatially averaged ripples (η and η/λ, Table 2), $d_{0s}/2k_s$ was found to be 10.84, 11.58, and 12.15 during experiments M04, M05, and M06, respectively, which moves the classification more into the 3D realm (according to the parameterizations in Figure 1). It is concluded here therefore, that during M04 the rippled bed was dominantly 2D in form. During M05, however, 3D ripples started to emerge and the plan-form geometry of the bed is thus classified as quasi-2D [*Pedocchi and Garcia*, 2009]. During M06, the 3D ripples continued to emerge and became more dominant features on the bed, although there remained some remnants of the quasi-2D ripples. From these classifications of the plan-form geometry, it was concluded that the ripples beneath the ARP were sufficiently long-crested for them to be classified as locally two dimensional for the present analysis.

4.3. Suspended Sediments

[23] The root mean square (RMS) average voltage backscattered from the suspended sediments measured by the ABS transceivers can be expressed as [*Thorne and Hanes*, 2002]

$$V_{rms} = \frac{\langle f \rangle}{\sqrt{\langle a_s \rangle \rho_s}} \frac{k_t}{\psi r} M^{1/2} \mathrm{e}^{-2r(\alpha_w + \alpha_s)}, \tag{17a}$$

where

$$\alpha_s = \frac{1}{r} \int_0^r \frac{3\langle \chi \rangle}{4\langle a_s \rangle \rho_s} M(r) dr \tag{17b}$$

is the attenuation due to sediment. In equations (17a) and (17b) ψ accounts for the departure from spherical spreading in the near field of the transducers [*Downing et al.*, 1995], r is the range from the transducers, M is the mass concentration of the sediment, k_t is the ABS system constant, $\langle a_s \rangle$ is the mean radius of the suspended sediments, and α_w is the attenuation coefficient due to the water absorption. The brackets, $\langle\ \rangle$, indicate an average taken over the particle number size distribution of the suspended sediment. The

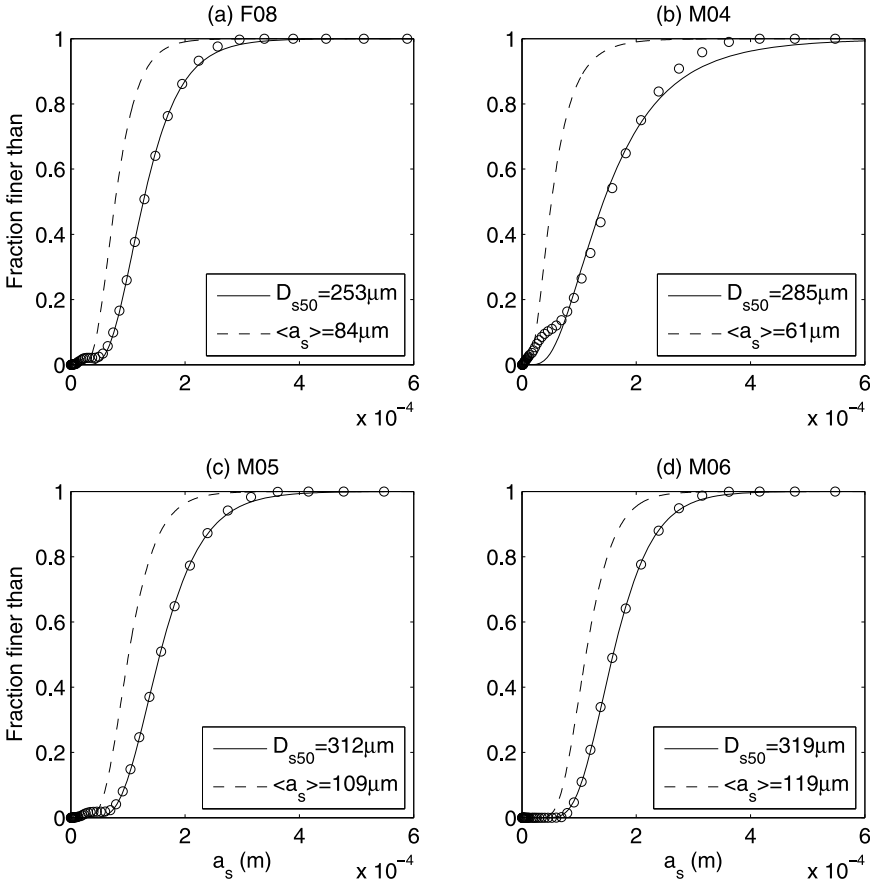

Figure 7. Lognormal mass concentration (solid curve) and particle number (dashed curve) grain size cumulative distributions fitted to the results from the grain size analysis of the pumped samples taken during the (a) plane bed and (b–d) rippled bed Deltaflume experiments. The median grain diameter, D_{s50}, of the mass distributions and the mean grain radius, $\langle a_s \rangle$, of the particle number distributions are indicated in each case.

functions f and χ describe the intrinsic backscattering and attenuation characteristics for narrowly sieved sediments [*Moate and Thorne*, 2009], expressions for which were chosen on the grounds that they represent natural sands [*Thorne and Meral*, 2008]. Solving equation (17) for the sediment concentration (M) at each range bin from the transceivers is nontrivial, as α_s is a function of M; thus, an inversion methodology is required.

4.3.1. Grain Size Distributions

[24] The type and width of the suspended sediment grain size distribution affects the backscattering and attenuation characteristics of the sediments, and can therefore strongly influence the acoustic ABS inversion [*Moate and Thorne*, 2009]. It is therefore important to represent the ensemble scattering characteristics of the suspension by averaging f and χ over the particle number size distribution present in suspension, to obtain $\langle f \rangle$ and $\langle \chi \rangle$. In this study, the near-bed SSC is of primary importance and within the bottom 0.25 m of the bed the suspended median grain diameter, D_{s50}, of the pumped samples collected was nominally uniform with height above the bed. Hence the mass size distributions from the lower three pump sampling nozzles (typically within 0.25 m of the bed) were combined for each experiment. These mass size distributions of the pumped samples were found to be lognormal in form. Figure 7 shows the cumulative size distribution of the mass concentration (open circles) of the combined pumped sampled results for each experiment. Fitted to this data are lognormal cumulative distribution functions with their D_{s50} values indicated. To obtain $\langle f \rangle$ and $\langle \chi \rangle$ for the acoustic inversion, the mass size distributions were converted to particle number size distributions, the cumulative distribution functions of which are also shown in Figure 7 with their arithmetic means, $\langle a_s \rangle$, indicated. These lognormal size distributions (Figure 7) were characterized by their standard deviation to mean ratios, $\sigma/\langle a_s \rangle$, of 0.42, 0.64, 0.39, and 0.35 for experiments F08, M04, M05, and M06, respectively. Thus, the ensemble backscattering and attenuation characteristics of the suspended sediment, $\langle f \rangle$ and $\langle \chi \rangle$, were calculated by averaging f and χ over the lognormal size distributions of the suspended sediment described by the $\sigma/\langle a_s \rangle$ values.

4.3.2. Acoustic Inversion

[25] Initial explicit inversions [*Lee and Hanes*, 1995; *Thorne and Hanes*, 2002] for sediment mass concentration were performed on the RMS time average backscattered voltage from each transceiver. The RMS time averages were calculated over the time periods during which the pumped samples were taken and the pumped sampled (time averaged) sediment concentrations were used to constrain the explicit inversions. To further aid the inversions, the height

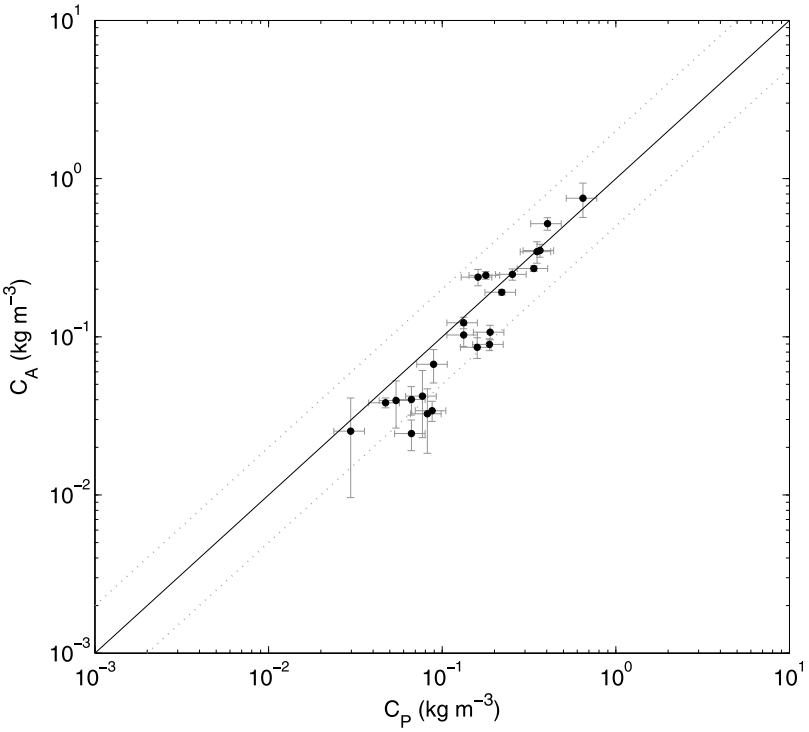

Figure 8. Regression plot of the mean time average ABS, C_A, and pumped sampled, C_P, suspended sediment concentrations with the curves corresponding to $C_A = C_P$ (solid curve) and $C_A = 2C_P$ and $C_A = 0.5C_P$ (dotted curves) shown. The error bars show ± the standard error of the mean of the three ABS frequencies for C_A and ±20% for C_P.

constant grain size profiles from the pumped samples were used. The grain sizes for each experiment were those indicated in Figure 7. In order to gain instantaneous concentration profiles, implicit inversions [*Thorne and Hanes*, 2002] for sediment mass concentration were performed on the 4 Hz ABS backscatter time series. The ABS system constant, k_t, required in the implicit inversions, for each of the three ABS transceivers was determined from the explicit inversion results. Thus, the implicit ABS inversions were linked to the pumped sampled concentrations from the four experiments.

[26] The implicit inversions resulted in time series of SSC profiles at 4Hz for each frequency. Mean time averages of these results were calculated for each experiment, and at each frequency, in order to test their validity against the independent pumped sampled measurements. Figure 8 shows the time-averaged sediment concentrations from the implicit inversions, C_A, compared with the concentrations obtained from the pumped samples, C_P. There are errors associated with both C_A and C_P. Concentration C_A is the mean of the inversion results from the three ABS frequencies. The error bars indicate the associated standard error. The indicated error on C_P is ±20%, which is the typical error found by *Moate and Thorne* [2009]. Sediment concentration estimates from the ABS is typically accurate to within a factor of two [*Vincent*, 2007] and the majority of data in Figure 8 falls within that range. A regression on the data in Figure 8 gave $C_A = (1.18 \pm 0.14)\ C_P - (0.05 \pm 0.03)$ with $R^2 = 0.93$. This regression and Figure 8 both confirm the veracity of the ABS measurements of suspended sediment concentration.

4.3.3. Time-Averaged SSC Profiles

[27] Figure 9 shows the time-averaged SSC profiles, $C(z)$, obtained from the calibrated implicit inversions. The three profiles obtained above the rippled beds (M04–M06) are similar in form and generally increase in magnitude with the significant wave height. All three rippled bed SSC profiles in Figure 9 exhibit a near-exponential decay, of similar gradient, within the bottom 15 cm. An exponential function, of the form given by equation (8), was fitted to the concentration measurements within 0.02–0.12 m above the bed level. In the rippled bed cases, the resulting exponential decay length scales, L, were between 0.06 and 0.07 m and the reference concentrations, C_0, obtained by extrapolating to the bed level, were between 1.5 and 2.2 kg m^{-3}. These observations of C_0 are somewhat below predictions made using equation (10) of *Nielsen* [1986], but are broadly within the scatter of data used by *Nielsen* [1986].

[28] Predictions were made of the SSC profiles using equation (8) with L predicted by the formula of *Nielsen* [1992] (equation (11)) and C_0 values from the data. In evaluating equation (11), the hydrodynamic (U_{0s}) and bed (η_0) conditions in Tables 1 and 2 were used along with the formula of *Soulsby* [1997] (equation (12)) for the sediment settling velocities. In order to include the effect that the grain size distribution had on the SSC profiles, the settling velocity distribution was taken into account using the method outlined by *Davies and Thorne* [2002]. The size distributions of the suspended sediment (Figure 7) were divided into five volumetrically equal fractions and the SSC profile for each of these fractions calculated. For all but the finest fraction in each case $U_{0s}/w_s < 18$, and in equation (11)

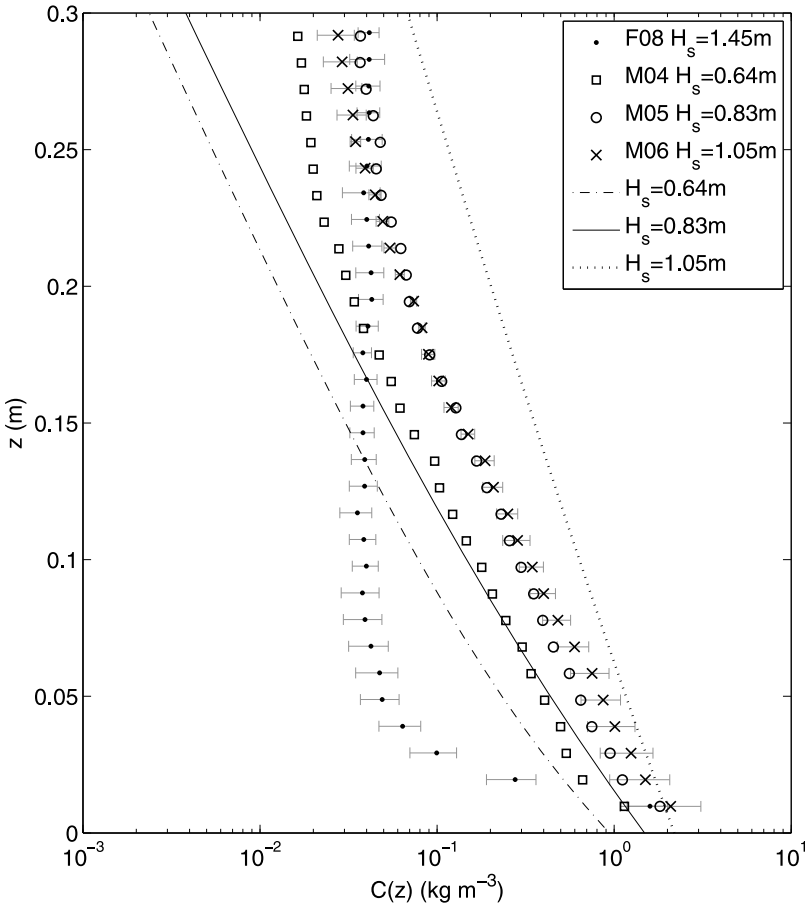

Figure 9. Suspended sediment concentration profiles, $C(z)$, for each experiment, mean time averaged over 17 minutes during which the pumped samples were collected, and mean averaged over the three ABS frequencies. The standard error of the mean of the three ABS frequencies is shown as error bars for the measurements taken during F08 and M06 in order to indicate typical measurement uncertainty through the profile. The empirical suspended sediment concentration (SSC) profile of *Nielsen* [1986] is shown for each rippled bed experiment, M04 (dash-dotted curve), M05 (solid curve) and M06 (dotted curve).

L was a function of U_{0s}. The predictions of the SSC profiles above the rippled beds included in Figure 9 are the mean averages of the profiles calculated for each of the five size fractions. There is a slight departure from the exponential decay of equation (8) due to the inclusion of the settling velocity distribution. The characteristic decay length scale of these predicted profiles differed from those observed by up to 40%. One reason for the disagreement between the predictions and observations of C_0 and L is the variation in velocity amplitudes from wave-to-wave, that is, U_{0s} may not be a good representative velocity for the irregular wave field. This variation in U_0 from wave-to-wave influences the sediment entrainment process, which is the investigative focus of this paper. Whether the entrainment of sediment was dominated by the same process during the whole time period that the SSC profiles in Figure 9 were averaged over is an important consideration.

4.4. Intrawave Water Velocities

[29] The bed level during each experiment obtained from the ARP and ABS records were in agreement and indicated that the sampling volumes of ADV-1 and ADV-2 were approximately 0.5 and 0.1 m above the bed, respectively, during the course of the rippled bed experiments (M04–M06). During the fine-medium-grained plane bed experiment, F08, the instrument frame settled into the bed such that the sampling volume of ADV-1 was 0.35 m above the bed and that of ADV-2 was below bed level. Hence no data from ADV-2 gathered during F08 were used. For the rippled bed experiments, the near-bed velocities from ADV-2 were used to identify the wave cycles in the phase-locking analysis of the SSC time series (section 4.5). In the case of F08, where the sampling volume of ADV-2 was below bed level, velocity data from ADV-1 were used.

[30] Each time series component (obtained from the ADVs at 16 Hz) was despiked using a phase-space thresholding method [*Goring and Nikora*, 2002] with detected spikes replaced by linear interpolations using the surrounding data points and run for 10 iterations. The velocity components were rotated to correct for any misalignment of the instruments with the main flow directions. This was done by considering each combination of two velocity components in turn and then aligning one of the components with the principle axis of variation [*Emery and Thompson*,

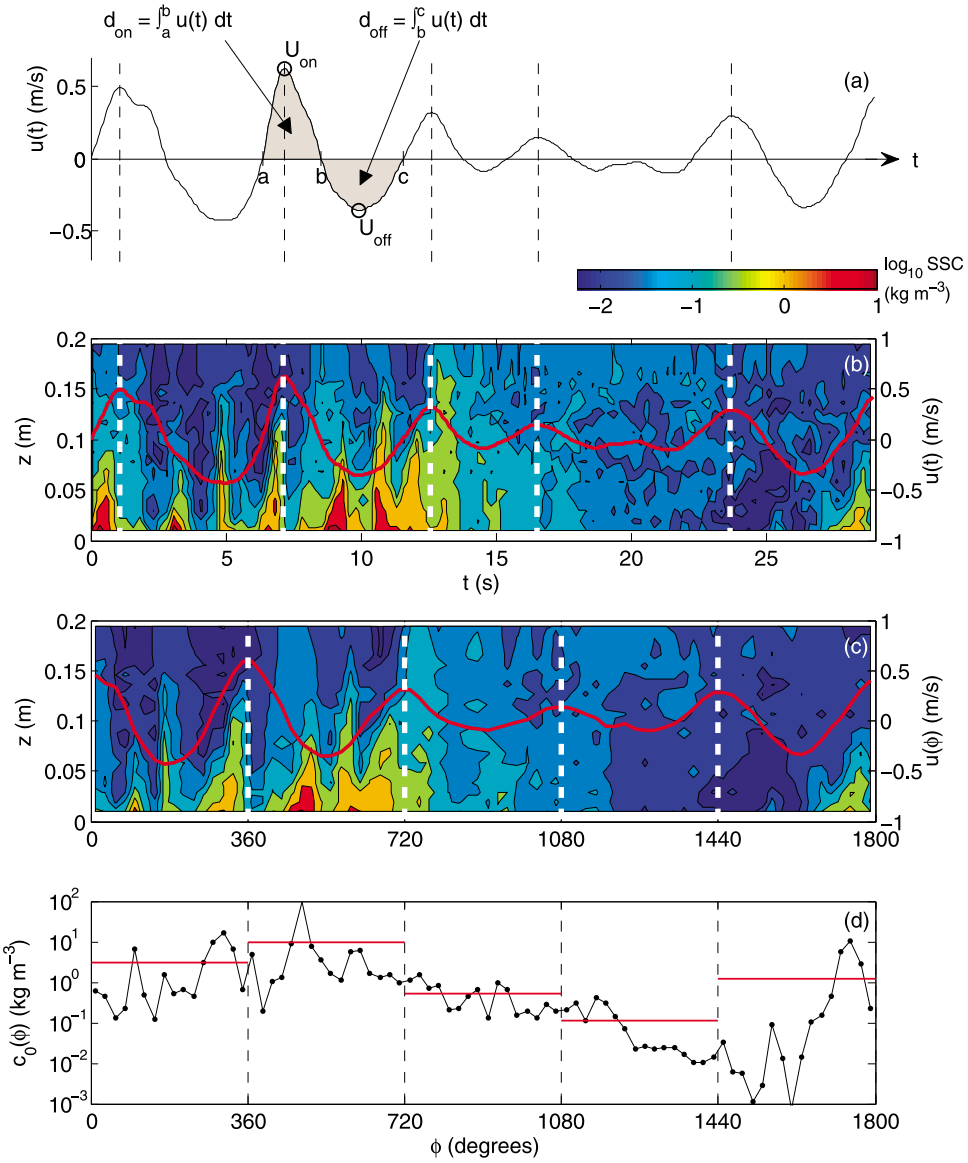

Figure 10. Five wave cycles (~30 s) from M04 of (a) filtered ADV-2 velocity time series, (b) SSC in the time t domain, (c) SSC in the phase ϕ domain, and (d) instantaneous reference concentration, $c_0(\phi)$, as a function of ϕ. Each wave cycle is indicated by vertical dashed lines. In Figure 10a the onshore and offshore orbital amplitudes, U_{on} and U_{off}, respectively, and onshore and offshore orbital diameters, d_{on} and d_{off}, respectively, are defined for the second wave cycle. In Figures 10b and 10c the orbital ADV velocity, u, from Figure 10a is overlain. In Figure 10d the cycle mean reference concentration, $\overline{c_0(\phi)}$, for each wave cycle is shown in red.

1997]. The result was a fully rotated system of three orthogonal velocity components. Here, positive water particle velocities corresponding to the direction of wave propagation are referred to as onshore velocities and negative water particle velocities toward the wave generator as offshore velocities. Following this convention the horizontal along-flume velocity component is referred to here as the cross-shore component.

[31] In order to determine the timing of each wave half cycle accurately, turbulent fluctuations were removed from the cross-shore ADV velocity time series by applying a rectangular low-pass filter and a zero-crossing analysis was used to identify the times of flow reversal. These filtered time series were compared with the nonfiltered time series confirming that no significant changes in amplitude and phase of the velocities occurred during the analysis. The zero-up crossings were defined as the start of each wave cycle, and the orbital velocity amplitudes and orbital diameters corresponding to each wave half cycle were sought. The velocity amplitudes were taken as the maximum velocity magnitude between successive zero-crossings, and the onshore and offshore velocity amplitudes, U_{on} and U_{off} respectively, were distinguished from one another. Figure 10a shows approximately 30 seconds of the filtered ADV-2 velocity time series from M04 with the U_{on} and U_{off} values for the second wave cycle indicated. The

orbital diameters were calculated by integrating the velocity time series between successive zero-crossings, and the onshore and offshore values, d_{on} and d_{off}, respectively, were distinguished from one another. For example, in Figure 10a a zero-up crossing occurs at time a, the subsequent zero-down crossing occurs at time b, and the orbital diameter corresponding to this onshore wave half cycle can be calculated by

$$d_{on} = \int_a^b u(t)dt, \tag{18}$$

where $u(t)$ is the time series of velocity, with $u(t) > 0$ in the onshore direction. The orbital diameter corresponding to the subsequent offshore wave half cycle is calculated in a similar manner, as indicated in Figure 10a. This approach was taken because the flow was irregular. If the flow was sinusoidal with period T and a velocity amplitude of U_0, that is, if $u(t)$ was replaced with $U_0\sin(2\pi t/T)$, then equation 18 would be equivalent to the more familiar equation of linear wave theory, U_0T/π. Following this zero-crossing analysis, a distribution of onshore and offshore velocity amplitudes (U_{on} and U_{off}, respectively) and orbital diameters (d_{on} and d_{off}, respectively) were constructed for each experiment.

4.5. Phase Ensemble Averaging the SSC

[32] There is inherent variability in the ABS signal due to the random, Rayleigh distributed, phasing of the acoustic returns [*Thorne et al.*, 1993]. This variability in the backscatter signal was reduced significantly by averaging over 32 independent measurements of acoustic backscatter, thus reducing the backscatter signal from 128 Hz to 4 Hz. The standard error on such an average is a factor of $\sqrt{32}$ smaller than if no averaging were performed [*Thorne and Hanes*, 2002].

[33] Small scale sediment transport processes are highly influenced by the turbulent nature of the boundary layer flow over rough beds; hence, there is an intrinsic stochastic variability in the SSC field. This is the case under both regular and irregular waves, but in the case of irregular waves there is considerable variance in the near-bed turbulence from wave-to-wave [*Vincent and Hanes*, 2002]. In order to observe consistent features in the intrawave SSC field, ensemble averaging over a number of wave cycles was therefore necessary.

[34] Figure 10b shows a series of SSC profiles, with the height above the bed, z, ranging from 0 to 20 cm, during five wave cycles (approximately 30 s) of M04 in the time domain, with the filtered ADV velocity from Figure 10a superimposed. Each wave cycle was identified from the zero-crossing and turning point time series analysis of the filtered ADV velocity, and the wave cycles are distinguished in Figures 10a and 10b. Each wave cycle was defined to start at the point of maximum velocity in the onshore (positive) direction. Using this definition allowed the sediment dynamics occurring around flow reversal to be clearly observable within the wave cycle. The wave irregularity can be observed in Figures 10a and 10b, both in terms of the wave amplitude and the wave period. Because the wave period varied from wave-to-wave, it was not possible to simply ensemble average over recurrent time steps equal to the wave period, as has been carried out under regular oscillatory flow [*Davies and Thorne*, 2005; *van der Werf et al.*, 2007]. Instead a procedure phase-locking the ABS concentration profiles with the ADV orbital velocities was performed, so that the ensemble averaging could be carried out in the phase domain rather than the time domain. Figure 10c shows the same series of SSC profiles and ADV velocities as Figure 10b, but in the phase domain, and again, the wave cycles (now equally spaced) are indicated. The resolution of the phase domain was 22.5° (16 SSC profiles per wave cycle). Figure 10c shows five wave cycles of SSC profiles in the phase domain for illustration only. The SSC profile series considered for each experiment were the bursts identified in section 4.2 during which the ABS was over a ripple crest. There were between 50 and 100 wave cycles in the SSC profile series for each rippled bed experiment, depending on the length of the measurement burst. Figure 10d shows the instantaneous reference concentration, $c_0(\phi)$, for five wave cycles and will be discussed in section 4.6.

[35] Figure 11a and Figures 11b–11d present the SSC results above the flat bed and the three rippled beds, respectively, phase ensemble averaged over the measurement bursts. Figures 11a–11d show the underlying intrawave variation of the SSC with height above the bed and Figure 11e shows the corresponding phase ensemble averaged orbital velocity, $\langle u \rangle$, for each experiment. There is a clear difference between the structure of the SSC field during the flat bed (Figure 11a) and rippled bed experiments (Figures 11b–11d). Above the flat bed, the sediment concentration is high in the bottom 2 cm and decays abruptly above this. There is also no significant intrawave variation in the SSC. Conversely, above the rippled beds the concentration decay rate is more gradational with distance from the bed and there is a clear intrawave structure present with peaks in the sediment concentration occurring around flow reversal (90° and 270°). The intrawave structure of the SSC is most similar during experiments M04 (Figure 11b) and M05 (Figure 11c) with the peaks in the concentration occurring at the same phase angles and the concentrations throughout the wave cycle being comparable. During M06 (Figure 11d), the sediment concentration peaks earlier in the wave cycle than during the previous two experiments. In terms of SSC magnitude, at one ripple height above the rippled beds, the concentration peaks are between 1.01 and 1.85 kg m^{-3} near the instances of flow reversal and consistently drop to below 0.34 kg m^{-3} near the instances of maximum velocity.

4.6. Bed Levels and Reference Concentrations

[36] The ABS system allows for the accurate identification of the bed level directly below the transducers, knowledge of which is crucial for studying the dynamics of near-bed sediment suspensions. Measurement bursts were considered when a ripple crest was below the ABS and the bed levels were constant in time, that is, when there was no ripple migration or bed evolution. These ABS backscatter time series were compared across all three frequencies and were found to increase exponentially toward the bed. The bed level was taken at the level of the first measurement significantly larger than the exponential trend. The instantaneous reference concentration as a function of phase, $c_0(\phi)$, where ϕ is the phase angle, was taken at the bed level,

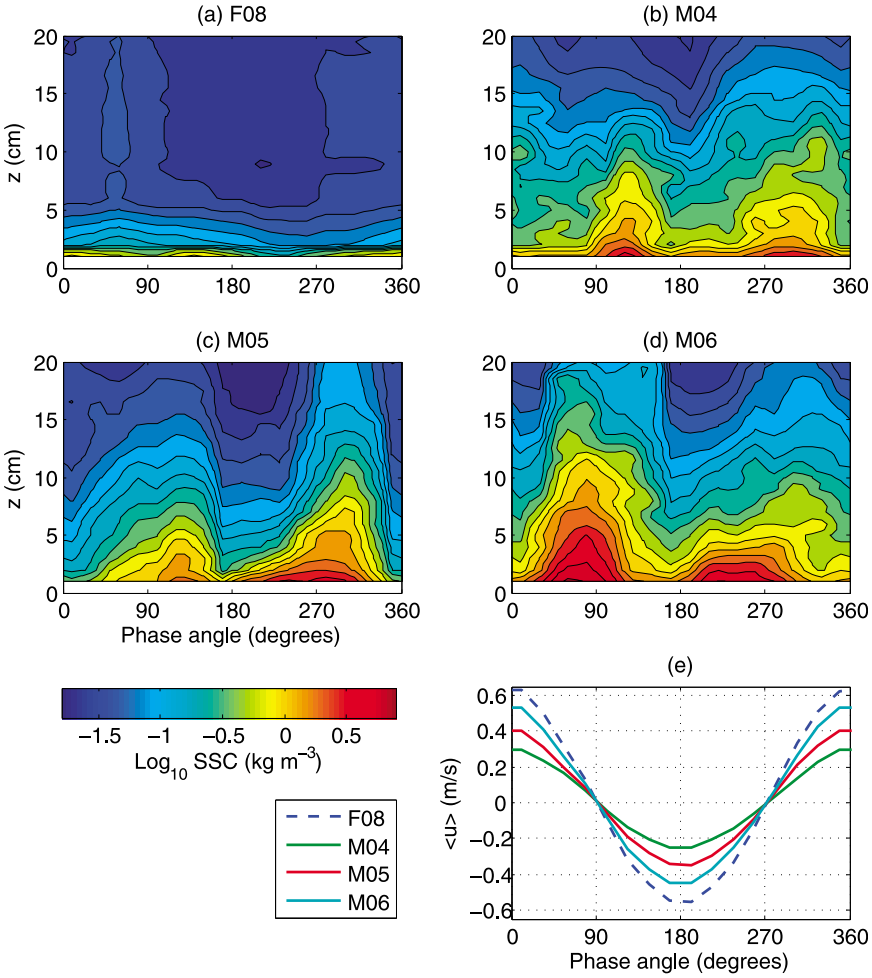

Figure 11. Intrawave variation in SSC with height above the bed, z, phase-locked to the near-bed velocities and phase ensemble averaged over the bursts during (a) plane and (b–d) rippled bed conditions. (e) Ensemble averaged intrawave near-bed velocity, $\langle u \rangle$, for each experiment. The results shown are the mean concentrations from the 1 and 2 MHz ABS frequencies.

which in the cases of the rippled beds was approximately the ripple crest level. An exponential function, of the form given in equation (8), was fitted to the measurements of the SSC within 0.02–0.05 m above the bed level, and $c_0(\phi)$ was obtained by extrapolation to the crest. This was done for each concentration profile within the 16 profiles per wave cycle phase-series as described in section 4.5. Figure 10d shows the calculated instantaneous reference concentration as a function of phase ($c_0(\phi)$) for five wave cycles. For each wave cycle, the cycle mean reference concentration, $\overline{c_0(\phi)}$, where the over bar indicates an average over the wave cycle, is indicated. The $\overline{c_0(\phi)}$ values were used to normalize the instantaneous intrawave $c_0(\phi)$ values within each wave cycle. This normalization from wave-to-wave within the irregular wave sequence enabled the underlying structure of the intrawave reference concentration to be studied.

[37] Figure 12 shows the phase ensemble averaged normalized intrawave reference concentrations, $\langle c_0(\phi)/\overline{c_0(\phi)} \rangle$, for each experiment, where the brackets, $\langle\ \rangle$, indicate phase ensemble averaging over 50–100 wave cycles and the error bars show the standard error of the ensemble averages. Considering the relative size of peaks in $\langle c_0(\phi)/\overline{c_0(\phi)} \rangle$ and the associated standard error, during an average wave cycle the rippled bed cases (Figures 12b–12d) show two distinct peaks occurring around flow reversal (90° and 270°). Conversely, the flat bed case has smaller peaks occurring around peak flow when the shear stress is highest over the plane bed (Figure 12a). The relative amplitude of the peaks in the rippled bed experiments compare well and the timing of the peaks in experiments M04 and M05 compare well (with peaks occurring 24° (onshore) and 11° (offshore) after flow reversal). The peaks in $\langle c_0(\phi)/\overline{c_0(\phi)} \rangle$ during M06, on the other hand, preceded flow reversal by 34°.

[38] Net suspended sediment flux calculations crucially depend on the magnitude of the SSC in suspension which, in turn, depends on the reference concentration (i.e. equation (8)). Under irregular waves the instantaneous reference concentration, $c_0(\phi)$, and hence the cycle mean, $\overline{c_0(\phi)}$, varies from wave-to-wave. Thus, the prediction of $c_0(\phi)$ under irregular waves is important in the modeling of SSC profiles within wave resolving process models such as the 'research' models studied by *Davies et al.* [2002].

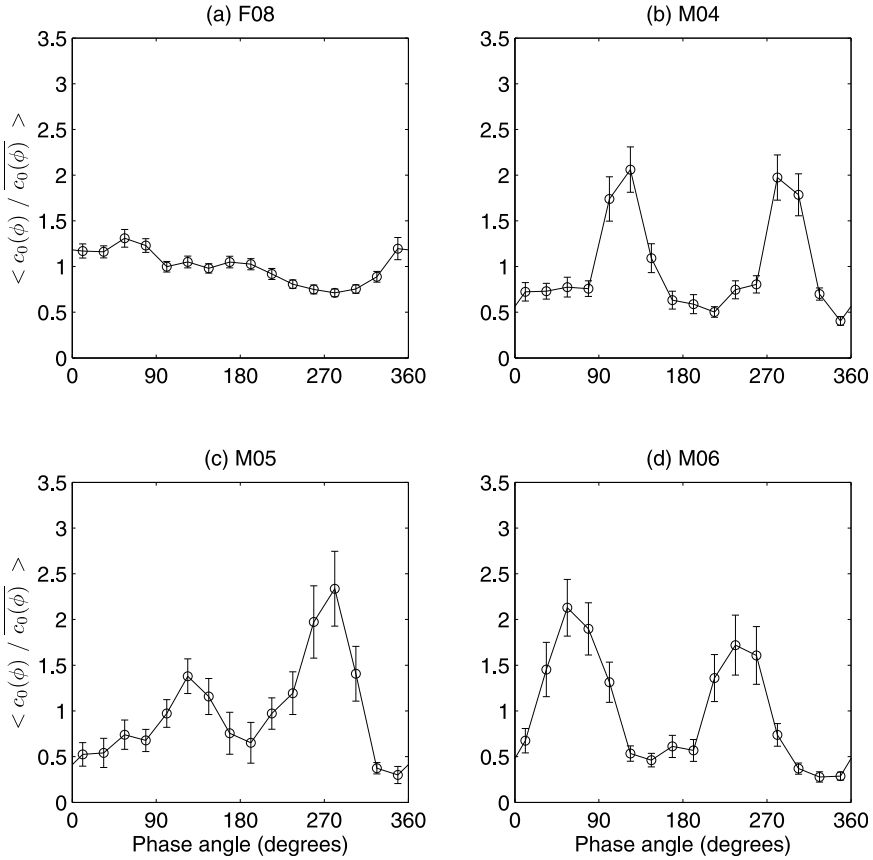

Figure 12. Phase ensemble averaged normalized intrawave reference concentrations, $\langle c_0(\phi)/\overline{c_0(\phi)}\rangle$. The ensemble averaging, $\langle\ \rangle$, is over all wave cycles during (a) plane and (b–d) rippled bed conditions. The error bars show the standard error of the ensemble averaging. Both $c_0(\phi)$ and $\overline{c_0(\phi)}$ were calculated from mean concentration values from the 1 and 2 MHz ABS frequencies.

[39] Here, for irregular waves, an approach similar to the time average analysis used by *Nielsen* [1986] is adopted for a wave-by-wave analysis. For each wave cycle, the cycle mean ripple modified Shields parameter, $\overline{\theta}_r$, was calculated using equation (9), and by taking the wave orbital amplitude and diameter for each wave cycle, U_0 and d_0 respectively, as the mean of the two half cycles, that is, $U_0 = \frac{1}{2}(U_{on} + U_{off})$ and $d_0 = \frac{1}{2}(d_{on} + d_{off})$. Figure 13 shows the cycle mean reference concentration, $c_0(\phi)$, from each of the three rippled bed experiments (M04–M06) plotted against $\overline{\theta}_r$ along with the empirical equation of *Nielsen* [1986] (equation (10)). The $\overline{c_0(\phi)}$ values shown are the mean of the values obtained from the results of the 1 and 2 MHz ABS frequencies and the error bars show the standard error of the mean. The error bars of the $\overline{\theta}_r$ values are the result of propagating the standard error of each quantity though equation (9). The majority of the data compares reasonably well with the equation of Nielsen, though with a few outliers. These outliers tend to correspond to wave half cycles where $d_0/\lambda_0 < 1$, below which flow separation is not expected to occur [*Malarkey and Davies*, 2002], and are indicated in Figure 13 with open circles. A linear regression has been made in log-log space on $\overline{c_0(\phi)}$ and $\overline{\theta}_r$, where $d_0/\lambda_0 \geq 1$, yielding

$$\overline{c_0(\phi)} = (0.0116 \pm 0.0034)\rho_s \overline{\theta}_r^{3.50\pm0.32}, \qquad (19)$$

with a correlation coefficient $R^2 = 0.78$. Equation (19) broadly agrees with the equation of *Nielsen* [1986] (equation (10)), in terms of the approximate cubic relation between $c_0(\phi)$ and θ_r. The coefficient is somewhat larger than that of Nielsen. The difference between equation (19) and that of *Nielsen* [1986] may be due to the fact that cycle mean reference concentrations, rather than time average reference concentrations, are presented here and that our regression was on data where $d_0/\lambda_0 \geq 1$.

5. Investigating the Vortex Shedding Regime

[40] Equation (7) relates the relative roughness of the bed, $d_0/2k_s$, to the parameter d_0/λ which *Malarkey and Davies* [2002] used as a parameterization of the sediment suspension process, namely vortex shedding. The $d_0/2k_s$ values of the rippled bed found in section 4.2 fall within the secondary vortex shedding criteria of *Malarkey and Davies* [2002] suggesting that vortex shedding should have occurred during these experiments.

[41] The peaks in the ensemble averaged intrawave SSC in Figure 11 and the reference concentration in Figure 12 coincide. Over the rippled beds, these peaks occur around flow reversal and can be interpreted as a signature of flow separation and the process of vortex shedding. Figures 11 and 12 are phase ensemble averages over full wave cycles

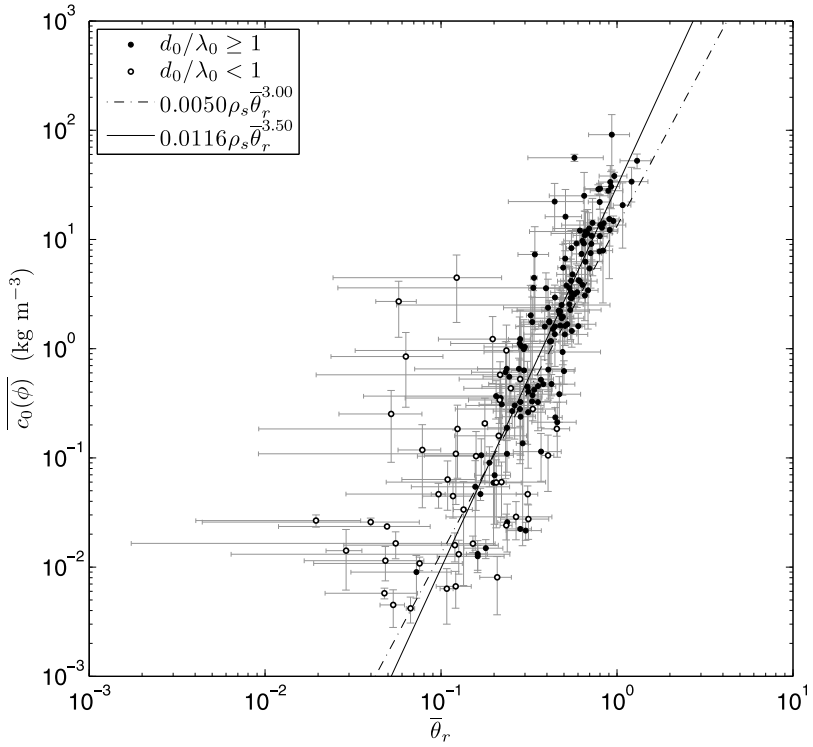

Figure 13. Wave cycle mean reference concentrations, $\overline{c_0(\phi)}$, during the rippled bed experiments against the wave cycle averaged ripple modified skin friction Shields parameter, $\overline{\theta}_r$. The $\overline{c_0(\phi)}$ is the mean of the results from the 1 and 2 MHz ABS frequencies and the error bars are the associated standard error. The error bars for $\overline{\theta}_r$ shows the standard error due to the wave asymmetry and the uncertainty in ripple steepness. Those points corresponding to wave half cycles where $d_0/\lambda_0 < 1$, where $d_0 = \frac{1}{2}(d_{on} + d_{off})$ and λ_0 is the wavelength of the ripple below the ABS, are indicated with open circles. The predictor of *Nielsen* [1986] is shown (dash-dotted curve) together with the results of a regression analysis (solid curve) performed on those values corresponding to wave half cycles where $d_0/\lambda_0 \geq 1$.

and indicate the average response of the suspended sediments to the irregular wave forcing. Under regular waves, ensemble averaging helps to reveal the underlying sediment transport phenomena, due to the sediment entrainment process being repeated every wave cycle. However, under the irregular waves used in the present study, the situation was more complicated since each wave was different and therefore less consistency was expected in the suspended sediment field from wave-to-wave. The reason for this variability between wave cycles was because the d_0/λ parameter varied from wave-to-wave and was not sufficient under every wave for the vortex shedding process to occur (i.e. the vortex shedding criteria of *Malarkey and Davies* [2002]), $1 \leq d_0/\lambda \leq 4$, was not fulfilled under every wave. This can alternatively be thought of as a disequilibrium between the flow and bed forms during some wave cycles. Despite this, the ensemble averaged results in Figures 11 and 12 show an intrawave variation of the suspended sediment field consistent with that which occurs above ripples and under regular oscillatory flow on average [i.e. *Davies and Thorne*, 2005; *van der Werf et al.*, 2007]. However, one must be aware that the ensemble average results (Figures 11 and 12) have been phase ensemble averaged over both vortex shedding and nonvortex shedding events, but that the vortex shedding events dominate and are thus revealed through ensemble averaging.

[42] In this section, the dependence of vortex shedding on the parameter d_0/λ, inherently linked to the relative roughness of the bed (equation (7)), is investigated by examining the phase ensemble averaged intrawave variations in the reference concentration during a number of intervals of d_0/λ_0, where d_0 refers to either d_{on} or d_{off} and λ_0 is the measured wavelength of the ripple below the ABS (Table 2).

[43] For each of the three rippled bed experiments the distributions of d_0/λ_0 were divided into classes of width $d_0/\lambda_0 = 0.2$. Phase ensemble averages of $c_0(\phi)/\overline{c_0(\phi)}$ were taken over the wave half cycles within each class to yield phase ensemble averages over half wave cycles within a discrete class of d_0/λ_0. This was carried out for both for onshore (d_{on}/λ) and offshore (d_{off}/λ) distributions and for each of the three ripple bed experiments in turn. By examining $\langle c_0(\phi)/\overline{c_0(\phi)}\rangle$ in each discrete class of d_0/λ, it was identified that the vortex shedding signature, identified as a distinct peak in $\langle c_0(\phi)/\overline{c_0(\phi)}\rangle$ around flow reversal, was consistently only present in those classes where $d_0/\lambda_0 \geq 1.2$. This was true for both onshore and offshore wave half cycles. Figures 14a–14d show phase ensemble averages of the normalized reference concentration for onshore and offshore wave half cycles where $d_{on/off}/\lambda_0 < 1.2$ and $d_{on/off}/\lambda_0 \geq 1.2$. The upper limit, at which vortex shedding ceases to occur, has not been examined because there were insufficient wave half cycles where $d_0 > 4\lambda$ for any meaningful conclusions to

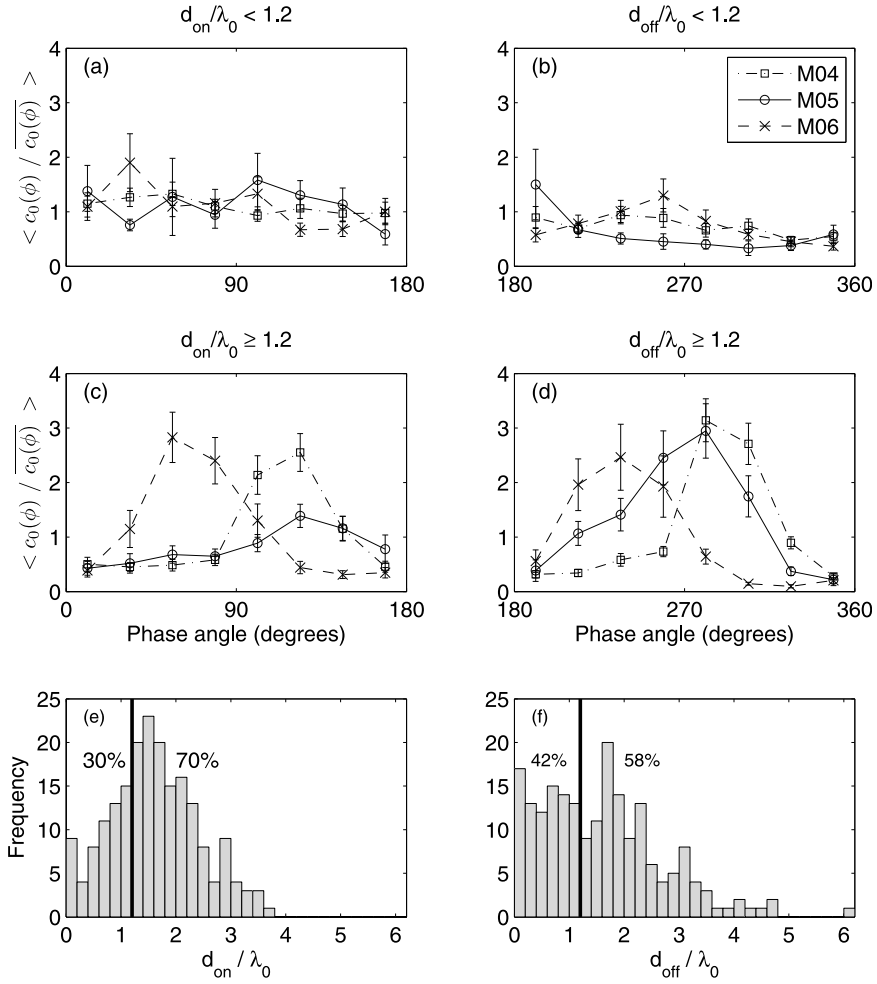

Figure 14. Phase ensemble averaged normalized intrawave reference concentrations, $\langle c_0(\phi)/\overline{c_0(\phi)}\rangle$. The ensemble averaging, $\langle\ \rangle$, is over wave half cycles where (a) $d_{on}/\lambda_0 < 1.2$, (b) $d_{off}/\lambda_0 < 1.2$, (c) $d_{on}/\lambda_0 \geq 1.2$ and (d) $d_{off}/\lambda_0 \geq 1.2$ for the three rippled bed experiments (M04–M06). The ensemble averaging was performed separately over the onshore (Figures 14a and 14c) and offshore (Figures 14b and 14d) wave half cycles and the error bars show the standard error of the ensemble averages. The distributions of (e) onshore and (f) offshore orbital diameter to ripple wavelength ratios, combined from the three rippled bed experiments, are shown with the d_{on}/λ_0 and $d_{off}/\lambda_0 = 1.2$ thresholds (black bin) and the percentage of waves on either side of the threshold indicated.

be drawn. When $d_0/\lambda_0 < 1.2$ (Figures 14a and 14b), $\langle c_0(\phi)/\overline{c_0(\phi)}\rangle$ shows no coherent structure through the wave half cycle, whereas when $d_0/\lambda_0 \geq 1.2$ (Figures 14c and 14d), $\langle c_0(\phi)/\overline{c_0(\phi)}\rangle$ exhibits distinct peaks around flow reversal. Therefore, $d_0/\lambda = 1.2$ is interpreted here as a threshold below which flow separation does not occur and above which it does and the process of vortex formation and shedding dominates the suspension of sediment. The combined distributions of d_{on}/λ_0 and d_{off}/λ_0 from each rippled bed experiment are shown in Figure 14e and Figure 14f, respectively. Also indicated is the threshold value of $d_0/\lambda_0 = 1.2$ above which vortex shedding has been assessed to occur. Approximately 70% of the onshore wave half cycles and 58% of the offshore wave half cycles fall above this threshold.

[44] Table 3 shows the results presented in Figures 14e and 14f for the three individual rippled bed experiments. These results suggest vortex shedding occurred approximately 12% more often around flow reversal after the onshore wave half cycles than after the offshore wave half cycles. This is most likely due to the asymmetry of the

Table 3. Percentage of Wave Half Cycles Assessed as Vortex Shedding[a]

				Wave Half Cycles Assessed as Vortex Shedding		
	d_{0s}/λ_0	$\overline{U_{on}}$	$\overline{U_{off}}$	Onshore %	Offshore %	Combined %
M04	2.55	0.31	0.26	66	53	60
M05	3.21	0.42	0.36	88	76	82
M06	1.89	0.55	0.47	60	49	54

[a]The onshore and offshore results for each experiment and the combined onshore and offshore results are shown for each experiment in the right-hand column. Mean onshore and offshore velocity amplitudes, $\overline{U_{on}}$ and $\overline{U_{off}}$, respectively, are shown along with the significant orbital diameter to ripple wave length ratio, d_{0s}/λ_0, for each experiment.

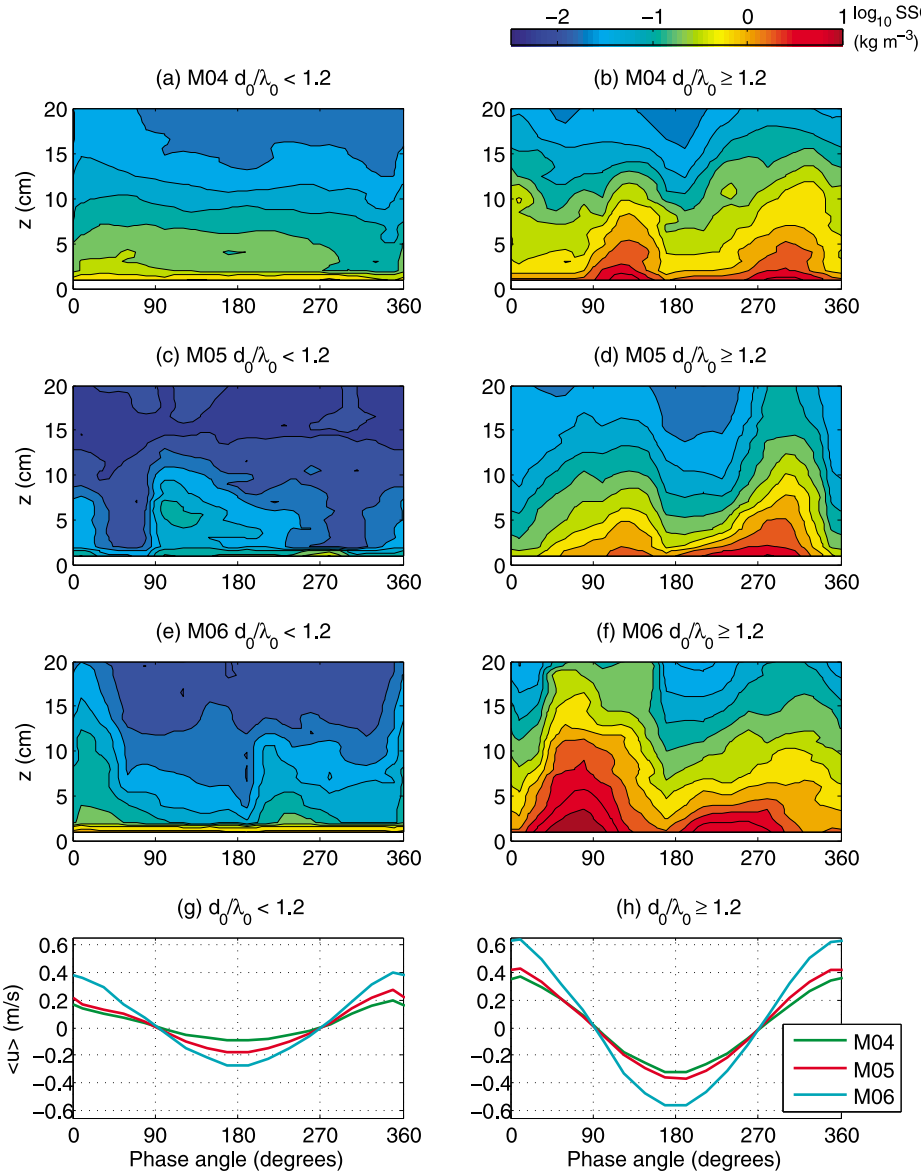

Figure 15. Intrawave variation in the SSC with height above the bed, z, phase locked to the near-bed velocities and phase ensemble averaged over wave cycles where (a, c, e) $d_0/\lambda_0 < 1.2$ and (b, d, f) $d_0/\lambda_0 \geq 1.2$ for rippled bed experiments M04 (Figures 15a and 15b), M05 (Figures 15c and 15d), and M06 (Figures 15e and 15f). Intrawave near-bed velocity ensemble averaged over wave cycles where (g) $d_0/\lambda_0 < 1.2$ and (h) $d_0/\lambda_0 \geq 1.2$ for the three experiments are shown.

velocity amplitude, evident in Figure 11e. To investigate this, the mean of the onshore and offshore velocity amplitudes were calculated ($\overline{U_{on}}$ and $\overline{U_{off}}$, Table 3). These results demonstrate the onshore velocity amplitude was on average 1.2 times larger across all three experiments. Such asymmetry in the velocity field, and the associated dominant sediment pickup after the onshore wave half cycles, has strong implications in terms of the net cross-shore sediment transport over vortex ripples. This is because the suspended sediment picked up after the onshore wave half cycle is transported offshore during the offshore wave half cycle [*Bijker et al.*, 1976].

[45] Whether the occurrence of vortex shedding can be related to statistical representations of wave forcing, such as H_s or d_{0s} obtained by spectral analysis of the velocity or surface wave fields, is an important issue as it has direct modeling implications. Table 3 shows d_{0s}/λ_0, where d_{0s} is the significant orbital diameter from Table 1, for each experiment. The fraction of wave half cycles where $d_{on}/\lambda_0 \geq 1.2$ or $d_{off}/\lambda_0 \geq 1.2$ were a consistent fraction of d_{0s}/λ_0. Taking the average of these fractions gives the percentage of wave half cycles where vortex shedding occurs as (26 ± 1) d_{0s}/λ_0.

[46] Finally, in order to further examine the threshold value of $d_0/\lambda = 1.2$ obtained through examination of the intrawave reference concentrations, phase ensemble averages of the SSC field were taken over wave cycles where $d_0/\lambda_0 < 1.2$ and $d_0/\lambda_0 \geq 1.2$, respectively, and where $d_0 = \frac{1}{2}(d_{on} + d_{off})$. Figures 15a, 15c, and 15e present the phase ensemble averages taken over wave cycles where $d_0/\lambda_0 <$

1.2 for experiments M04, M05, and M06, respectively, and show low values of SSC throughout the wave cycle and little intrawave variability. Figures 15b, 15d, and 15f present the phase ensemble averages taken over wave cycles where $d_0/\lambda_0 \geq 1.2$ for experiments M04, M05, and M06, respectively. When $d_0/\lambda_0 \geq 1.2$, a familiar intrawave structure similar to those shown in Figures 11b–11d is present with strong peaks in the SSC occurring around flow reversal, indicating vortex formation and shedding is occurring. Figures 15g and 15h present the phase ensemble average intrawave variation in the orbital velocities, $\langle u \rangle$, when $d_0/\lambda_0 < 1.2$ and $d_0/\lambda_0 \geq 1.2$, respectively, from which it can be seen that $d_0/\lambda_0 < 1.2$ represents the more quiescent wave cycles in the measurement bursts. The important feature present in Figure 15 is the clear difference in the phase ensemble averaged SSC fields, both in terms of magnitude and intrawave structure, between wave cycles where $d_0/\lambda_0 < 1.2$ and where $d_0/\lambda_0 \geq 1.2$. These results are consistent with the intrawave structure of the reference concentrations in Figure 14 and confirms that below irregular waves, $d_0/\lambda = 1.2$ is a suitable threshold above which vortex formation and shedding become the dominant mechanism of sediment suspension above ripples.

6. Discussion

[47] Four experiments conducted in the Deltaflume under irregular wave forcing have been presented. Particular attention has been paid to the wave forcing, bed forms, fluid velocities, suspended sediment concentrations, and reference concentrations. In particular, the variation of the suspended sediment fields and fluid velocities on an intrawave time scale were studied here. During the first experiment, where $D_{50} = 258$ μm, the significant wave height, H_s, was 1.45 m and the shallow (nonvortex shedding) ripples present during previous wave forcing regimes (with smaller H_s) were washed out. The sediment dynamics above this bed thus approached that of a dynamically (upper stage) plane bed. During the latter three experiments, where $D_{50} = 375$ μm and $H_s = 0.64$–1.05 m, a (steep sided vortex shedding) rippled bed formed. These four experiments were chosen primarily so that two contrasting bed and sediment dynamics regimes, from those portrayed in Figure 1, could be presented. The sediment dynamics under different dynamic, but not strongly contrasting, flow conditions were studied, under which substantial sediment transport was expected. F08 enabled the sediment dynamics above a plane upper-stage bed to be observed and contrasted with that occurring above the rippled beds of M04–M06.

6.1. Bed Forms

[48] During the measurement bursts considered there was little or no change in the bed morphology. For example, during the rippled bed bursts there was no significant ripple migration or evolution in terms of ripple amplitude or height changes. Why there was no ripple migration observed during these bursts is an obvious question especially as ripples were observed to migrate as much as one ripple wavelength in 17 minutes in the Deltaflume under regular waves [*Davies and Thorne*, 2005]. This is interpreted to be related to the irregular wave forcing. *Faraci and Foti* [2002] showed that the ripple migration rate is influenced by the irregularity of the flow and that higher migration rates occur under regular waves. *Traykovski et al.* [1999] found the average onshore migration rate of ripples in a field environment to be 24 cm d^{-1}. Such migration rates would be unobserved over the length of the bursts considered in these experiments; hence, the nonmigration of the ripples over these time scales is not unexpected. The irregularity of the waves also explains why there was little evolution of the ripple geometry during the measurement bursts here: under irregular waves, where there is less of a dominant orbital length scale than under regular waves, ripples tend to remain in an initial configuration or evolve more slowly than under regular waves [*Marsh et al.*, 1999].

[49] Orbital ripples scale with the diameter of orbital motion, d_0, close to the bed [*Clifton*, 1976]. While the ripples observed here lie in the suborbital regime [*Wiberg and Harris*, 1994], it is still useful to compare their wavelength to d_0, as d_0 has a strong influence on their geometry. *Miller and Komar* [1980] proposed that the wavelength of orbital ripples was $\lambda = 0.65d_0$ and *Wiberg and Harris* [1994] later reported $\lambda = 0.62d_0$. These two results give $d_0/\lambda = 1.5$ and 1.6 which are larger than the value of $d_0/\lambda = 1.2$ for the initiation of vortex shedding found here, but is well within the range of values where vortex shedding is expected, according to the criteria of *Malarkey and Davies* [2002]. The fact that the parameter d_0/λ can be used both for the prediction of bed morphology [*Miller and Komar*, 1980; *Wiberg and Harris*, 1994] and the process of sediment entrainment illustrates the inherent link between bed morphology and the sediment entrainment process. Furthermore, d_0/λ is inherently linked to the equivalent roughness of vortex ripples by equation (7).

[50] The bed roughness, which is heavily dependent on the ripple dimensions, is an important consideration when modeling boundary layer flows [*Davies and Thorne*, 2008] and, in many cases, must be predicted from knowledge of the predominant flow conditions and bed sediments. Thus, ripple geometry prediction under waves is an active research area and a number of prediction schemes and formulae exist, based on parameters such as the orbital diameter characterizing the flow [e.g., *Mogridge et al.*, 1994; *Wiberg and Harris*, 1994; *Soulsby and Whitehouse*, 2005]. It was interesting therefore to compare the results of such prediction schemes with the direct measurements of ripples here, to provide insight into the expected bed form and sediment suspension conditions under the Deltaflume oscillatory flow.

[51] The suborbital regime defined by *Wiberg and Harris* [1994] can be expressed as $1800 < d_0/D_{50} < 5500$. Ripples with d_0/D_{50} smaller than 1800 or larger than 5500 are therefore within the orbital and anorbital regimes, respectively. The d_{0s}/D_{50} values for the Deltaflume experiments are listed in Table 1 and show that the flat bed (F08) and rippled beds (M04–M06) are within the suborbital and anorbital regimes, respectively. Using the significant orbital diameters and peak spectral periods from Table 1, the prediction formulae of *Mogridge et al.* [1994], *Wiberg and Harris* [1994], and *Soulsby and Whitehouse* [2005] were applied to the flow conditions during the Deltaflume bursts to find expected values for the ripple dimensions, the ripple wavelength, height, and steepness. The results are listed in Table 4. In Table 4 λ_M, η_M, and η_M/λ_M are the dimensions of

Table 4. Predicted Ripple Dimensions Using the Formulae of *Mogridge et al.* [1994] (λ_M, η_M, and η_M/λ_M); *Wiberg and Harris* [1994] (λ_W, η_W, and η_W/λ_W); and *Soulsby and Whitehouse* [2005] (λ_S, η_S, and η_S/λ_S)

	λ_M (m)	η_M (m)	η_M/λ_M	λ_W (m)	η_W (m)	η_W/λ_W	λ_S (m)	η_S (m)	η_S/λ_S
F08	0.35	0.015	0.04	0.12	0.008	0.07	0.12	0.003	0.02
M04	0.43	0.088	0.21	0.40	0.067	0.17	0.35	0.053	0.15
M05	0.45	0.087	0.19	0.36	0.060	0.17	0.32	0.047	0.15
M06	0.45	0.073	0.16	0.31	0.049	0.16	0.29	0.039	0.14

the ripples according to the predictor of *Mogridge et al.* [1994], λ_W, η_W, and η_W/λ_W are the dimensions of the ripples according to the predictor of *Wiberg and Harris* [1994] and λ_S, η_S, and η_S/λ_S are the dimensions of the ripples according to the predictor of *Soulsby and Whitehouse* [2005]. All these predictors are based on large amounts of data, and should therefore be most comparable with the spatial and temporal averages of the ripple dimensions measured using the ARP, λ, η, and η/λ in Table 2. However, all the predictions of the ripple height were 1.2–3.5 times larger than the measured spatial and temporal averages (η, Table 2) and all the predictions of the ripple steepness were 1.5–2.3 times larger than η/λ (Table 2). Similarly, for the flow conditions during M04 and M05, the predictions of the ripple wavelengths were 1.4–2.0 λ. The predictions of the ripple wavelength during the M06 flow conditions were generally more accurate with values ranging from 0.9–1.4 λ. Finally, Table 4 shows the results using the flow conditions during F08, where a reasonably plane bed was known to exist. The results all predict shallow ripples with heights in the range 0.3–1.5 cm, an order of magnitude smaller than the ripples known to be present during the rippled bed experiments (M04–M06). However, the wavelengths of 0.12–0.35 m were significantly shorter than the long wavelength bed form observed in Figure 4a. Overall, the predictor of *Soulsby and Whitehouse* [2005] predicted ripple dimensions most in line with those observed here. The predicted ripple wavelengths were 0.9–1.4 λ, the predicted ripple heights were 1.2–2.1 η, and the predicted ripple steepness values were 1.5–1.7 η/λ. The discrepancy between the predicted and observed ripple dimensions is here attributed to the fact that only three rippled beds were examined here and that the significant wave orbital diameters and peak spectral wave periods from Table 1 are not necessarily the best parameterization of the irregular wave fields. Furthermore, *Hanes et al.* [2001] found that ripple measurements from three field campaigns were approximately within a factor of two of those given by ripple prediction schemes.

6.2. Timings of Peak Sediment Entrainment

[52] The most striking similarity between the three rippled bed experiments is the ensemble averaged intrawave SSC fields (Figures 11b–11d) and reference concentrations (Figures 12b–12d), in terms of timing and magnitude. It is well-established that under regular waves and over a bed with steep ripples, sediment laden vortices are ejected over the ripple crest around the instances of flow reversal and that peaks in the SSC occur at these times above the ripple crest [e.g., *Davies and Thorne*, 2005; *van der Werf et al.*, 2007]. Therefore, the clear peaks observed here, under irregular waves, in the ensemble averaged intrawave SSC (Figure 11) and reference concentrations (Figure 12) near the instants of flow reversal support the concept of the process of vortex shedding taking place under irregular waves.

[53] While peaks in the SSC occurred around flow reversal during each of the rippled bed experiments, there are differences in the precise timing of the SSC peaks. The phase at which $\langle c_0(\phi)/\overline{c_0(\phi)}\rangle$ peaks in M04 and M05 compare well and occur between 11°–24° after flow reversal, broadly agreeing with the results of *van der Werf et al.* [2007], whereas the $\langle c_0(\phi)/\overline{c_0(\phi)}\rangle$ peaks in M06 precede flow reversal by 34°. A similar phenomenon was observed above the crests of vortex ripples by *Block et al.* [1994] beneath regular waves in a large flume tank (97 m long). *Block et al.* [1994] observed the SSC to peak (1) 10°–20° after flow reversal when $\eta/\lambda = 0.16$ and $d_0/\lambda = 1.62$ and (2) 20° before flow reversal when $\eta/\lambda = 0.11$ and $d_0/\lambda = 2.63$. This phase shift was attributed to the difference in the d_0/λ parameterization [*Block et al.*, 1994]. The phase shift observed here between M04 and M06 is of a similar magnitude to that observed by *Block et al.* [1994], but the d_{0s}/λ_0 value during M06 is smaller than that during M04. The ripple measured below the ABS during M06 was larger than the majority of ripples present on the bed at the time. The bed morphology was also dominantly three-dimensional during M06 and the bed forms may not have been truly in equilibrium with the flow. Perhaps, therefore, the λ_0 length scale was an inappropriate choice for the case of the M06 experiment. Using instead the spatially averaged ripple wavelength, λ in Table 2, produces $d_{0s}/\lambda = 4.18$ which is larger than that during M04 and therefore more consistent with the result of *Block et al.* [1994].

6.3. Implications

[54] The occurrence of the process of vortex shedding is well-established under regular oscillatory flow [e.g., *Davies and Thorne*, 2005; *van der Werf et al.*, 2007] but is not well-verified under irregular waves at field scale. This work verifies, under field scale irregular waves, the process of vortex shedding not only occurs, but can be a dominant mechanism of sediment suspension during both onshore and offshore wave half cycles. When modeling sediment fluxes, the prediction of the sediment suspension under waves can have a profound effect, that is, wave asymmetry can lead to the process of vortex shedding encouraging offshore pumping of sediment [*Bijker et al.*, 1976; *Davies and Thorne*, 2008]. Such an asymmetry in the intrawave velocity was observed here contributing to 12% more vortices being generated during the onshore wave half cycles beneath irregular waves. Therefore it is important for the process of vortex shedding to be considered within models of larger scale sediment transport. Commonly, the only readily available information about the hydrodynamic and sediment transport regime at a field location is the wave climate which, for simplicity, is often expressed in terms of

the significant wave height H_s and peak spectral period T_p. Such a modeling approach is simplistic, but often necessary in otherwise computationally demanding wide area models. It is therefore useful for the relation between H_s and the process of sediment entrainment due to vortex shedding to be discussed. H_s can readily be used to estimate an equivalent significant velocity amplitude U_{0s} [*Wiberg and Sherwood*, 2008] or significant orbital diameter d_{0s} close to the bed, which in turn can be related to vortex shedding with the parameter d_{0s}/λ, where λ is the characteristic ripple wavelength. The dependency of the occurrence of vortex shedding on d_{0s}/λ has been examined here under irregular waves. It has been found that the percentage of waves assessed as vortex shedding approximately scales as 26 d_{0s}/λ over steep vortex ripples. Furthermore, d_{0s} can be directly related to the significant wave height and peak spectral period using a relation based on linear wave theory (equation (16)). Thus, these observations on the frequency of vortex shedding events under irregular waves could serve as a practical assessment of vortex shedding within sediment transport models reliant on parameters such as H_s.

7. Conclusions

[55] The results presented here were achieved by making acoustic measurements, on an intrawave time scale, of the sediment suspensions under JONSWAP irregular waves over both plane and rippled beds, under different significant wave heights. A striking difference between the intrawave structure of the suspended sediments over a plane bed and rippled beds was observed. Over the rippled beds, the results demonstrate a clear suspended sediment structure consistent with lee-wake vortex shedding previously observed under regular waves [*Davies and Thorne*, 2005]. Even though the significant wave height was different in each rippled bed experiment, the intrawave structure and magnitudes of the SSC were remarkably similar. This consistency is ascribed to the similarity in the bed forms present (namely ripples with $\eta/\lambda > 0.1$ where boundary layer separation and vortex shedding can occur) rather than simply the wave forcing. This study establishes that vortex shedding occurs under field scale irregular free surface waves, with vortex shedding occurring under a percentage of the waves that appears to scale with the ratio of significant orbital diameter to ripple wavelength, d_{0s}/λ, by a factor of ~26. Furthermore, it was consistently observed that around 12% more vortex shedding events occurred after onshore wave half cycles than after offshore wave half cycles. This was due to wave asymmetry, and could lead to substantial offshore suspended sediment transport over longer time scales than the duration of the experiment. *Malarkey and Davies* [2002] suggest $1 \leq d_0/\lambda \leq 4$, equivalently expressed as $4.3 \leq d_0/2k_s \leq 17.4$ using equation (4) with $\eta/\lambda = 0.12$ and $\alpha = 8$, as a vortex shedding regime. The lower limit was tested here under irregular waves and a threshold value $d_0/\lambda = 1.2$, above which vortex shedding was a dominant entrainment process, was found. These results could serve as a practical assessment of vortex shedding within sediment transport models reliant on parameters such as the significant wave height, which can be related to d_{0s}.

[56] The use of acoustics is proving to be a powerful tool in the study of near-bed sediment dynamics. These conclusions are based on results from one-dimensional, vertical, measurements, over ripple crests, of SSC and point measurements of the near-bed flow. In recent years, acoustic technology has advanced and it is now possible to make detailed, collocated, one-dimensional measurements of the bed, the flow, and the suspended sediments at high temporal and spatial resolutions [e.g., *Thorne et al.*, 2009b]. In the future, these techniques will be applied in increasingly more natural environments, such as large scale flumes, as well as the field. Further insight will be gained into the complex sediment transport processes occurring at small spatial and temporal scales within rough boundary layers predominant in the coastal marine environment.

Notation

Symbol	Description [dimensions] (typical units)
H_s	significant wave height [L] (m)
T_p	peak spectral wave period [T] (s)
d_0	wave orbital excursion diameter [L] (m)
d_{0s}	significant wave orbital excursion diameter [L] (m)
U_0	wave orbital amplitude [$L\ T^{-1}$] (m s^{-1})
U_{on}	onshore wave orbital amplitude [$L\ T^{-1}$] (m s^{-1})
U_{off}	offshore wave orbital amplitude [$L\ T^{-1}$] (m s^{-1})
U_{0s}	significant wave orbital amplitude [$L\ T^{-1}$] (m s^{-1})
h	water depth [L] (m)
λ	spatially and temporally averaged ripple wavelength [L] (m)
η	spatially and temporally averaged ripple height [L] (m)
η/λ	spatially and temporally averaged ripple steepness [−]
λ_0	temporally averaged wavelength of ripple below the ARP [L] (m)
η_0	temporally averaged height of the ripple below the ARP [L] (m)
η_0/λ_0	temporally averaged steepness of the ripple below the ARP [−]
k_s	equivalent roughness [L] (m)
$d_0/2k_s$	relative roughness [−]
θ	skin friction Shields parameter [−]
$\theta_{2.5}$	grain roughness Shields parameter based on $k_s = 2.5D_{50}$ [−]
θ_r	ripple modified Shields parameter [−]
$f_{2.5}$	wave friction factor based on $k_s = 2.5D_{50}$ [−]
$u_{*2.5}$	shear velocity (skin friction) calculated using $f_{2.5}$
s	ratio of sediment density to water density [−]
ρ_s	sediment density [$M\ L^{-3}$] (kg m^{-3})
g	acceleration due to gravity [$L\ T^{-2}$] (m s^{-2})
D_i	grain diameter for which i% of sediment is finer than [L] (μm)
D_{s50}	median grain diameter of suspended sediment mass size distribution [L] (μm)
a_s	grain radius [L] (μm)
$\langle a_s \rangle$	mean radius of the suspended sediment particle number size distribution [L] (μm)
D_*	dimensionless grain size [−]

$C(z)$ time average suspended sediment concentration profile [$M\,L^{-3}$] (kg m^{-3})
z height above bed [L] (m)
L vertical decay length scale [L] (m)
C_0 time averaged mass reference concentration [$M\,L^{-3}$] (kg m^{-3})
t time [T] (s)
ϕ phase angle (degrees). Peak onshore velocity of the ith wave cycle is defined to occur at $\phi = 360(i-1)$
$c_0(t)$ instantaneous reference concentration as a function of time, t, [$M\,L^{-3}$] (kg m^{-3})
$c_0(\phi)$ instantaneous reference concentration as a function of phase, ϕ [$M\,L^{-3}$] (kg m^{-3})
w_s sediment settling velocity [$L\,T^{-1}$] (m s^{-1})
υ kinematic viscosity of water [$L^2\,T^{-1}$] (m^2 s^{-1})
ψ near-field correction to spherical spreading [−]
$M(r)$ mass concentration of sediment as a function of range, r [$M\,L^{-3}$]
k_t ABS system constant [−]
f form function [−]
χ normalized total scattering cross−section [−]
α_s sediment attenuation [L^{-1}] (m^{-1})
α_w water attenuation [L^{-1}] (m^{-1})
C_A sediment concentration obtained from the ABS at the pumped sampled bin ranges [$M\,L^{-3}$] (kg m^{-3})
C_P sediment concentration obtained from the pumped samples [$M\,L^{-3}$] (kg m^{-3})
$u(t)$ velocity time series as a function of time [$L\,T^{-1}$] (m s^{-1})
$\langle u \rangle$ phase ensemble averaged intrawave velocity [$L\,T^{-1}$] (m s^{-1})
$\overline{c_0(\phi)}$ cycle mean reference concentration [$M\,L^{-3}$] (kg m^{-3})
$\overline{\theta}_r$ cycle mean ripple modified Shields parameter [−]
$\langle c_0(\phi)/\overline{c_0(\phi)} \rangle$ phase ensemble averaged normalized intrawave reference concentration [−]

[57] **Acknowledgments.** This work was supported by the European Union, through its access to large-scale facilities, and by the Natural Environment Research Council and the University of Liverpool for PhD funding. The authors thank J. J. Williams at Associated British Ports, U. K., who coordinated the Deltaflume experiments and Paul S. Bell and Benjamin D. Moate at the National Oceanography Centre for help with analyzing the flow and ripple data. We thank Stephen S. Flint at the School of Environmental Sciences, University of Liverpool, for his support. The constructive reviews from Peter Nielsen at the University of Queensland, Australia, and an anonymous reviewer are also much appreciated. We especially thank Alan G. Davies at the School of Ocean Science, Bangor University, Wales, for his many useful conversations and suggestions.

References

Allen, J. R. L. (1979), A model for the interpretation of wave ripple-marks using their wavelength, textural composition, and shape, *J. Geol. Soc.*, *136*, 673–682.

Allen, P. (1997), *Earth Surface Processes*, Blackwell Sci., Oxford, U.K.

Ardhuin, F., T. G. Drake, and T. H. C. Herbers (2002), Observations of wave-generated vortex ripples on the North Carolina continental shelf, *J. Geophys. Res.*, *107*(C10), 3143, doi:10.1029/2001JC000986.

Bagnold, R. A. (1946), Motion of waves in shallow water: Interaction between waves and sand bottoms, *Proc. Royal Society London Series*, *187*(1008), 1–15.

Bijker, E. W., E. van Hijum, and P. Vellinga (1976), Sand transport by waves, paper presented at 15th International Conference on Coastal Engineering, Honolulu, Hawaii.

Block, M. E., A. G. Davies, and C. Villaret (1994), Suspension of sand in oscillatory flow above ripples: discrete-vortex model and laboratory experiments, in *Sediment Transport Mechanisms in Coastal Environments and Rivers, Euromech 310*, edited by M. Blorgey et al., World Sci., Singapore.

Bosman, J. J., E. T. J. M. van der Velden, and C. H. Hulsbergen (1987), Sediment concentration measurement by transverse suction, *Coastal Eng.*, *11*, 353–370.

Carter, D. J. T. (1982), Prediction of wave height and period for a constant wind velocity using the JONSWAP results, *Ocean Eng.*, *9*, 17–33.

Clifton, H. E. (1976), Wave-formed sedimentary structures - a conceptual model, in *Beach and Nearshore Sedimentation*, edited by R. A. Davis and R. L. Ethington, pp. 126–148, Soc. Econ. Paleontol. Mineral., Tulsa, Okla.

Clifton, H. E., and J. R. Dingler (1984), Wave-formed structures and paleoenvironmental reconstruction, *Mar. Geol.*, *60*, 165–198.

Davies, A. G., and P. D. Thorne (2002), 1DV-Model of sand transport by waves and currents in the rippled bed regime, in *Coastal Engineering 2002*, vol. 3, pp. 2599–2611, World Sci., Cardiff, U.K.

Davies, A. G., and P. D. Thorne (2005), Modeling and measurement of sediment transport by waves in the vortex ripple regime, *J. Geophys. Res.*, *110*, C05017, doi:10.1029/2004JC002468.

Davies, A. G., and P. D. Thorne (2008), Advances in the study of moving sediments and evolving seabeds, *Surv. Geophys.*, *29*, 1–36.

Davies, A. G., and C. Villaret (1999), Eulerian drift induced by progressive waves above rippled and very rough beds, *J. Geophys. Res.*, *104*, 1465–1488, doi:10.1029/1998JC900016.

Davies, A. G., and A. C. Villaret (2002), Prediction of sand transport rates by waves and currents in the coastal zone, *Cont. Shelf Res.*, *22*, 2725–2737.

Davies, A. G., J. S. Ribberink, A. Temperville, and J. A. Zyserman (1997), Comparisons between sediment transport models and observations made in wave and current flows above plane beds, *Coastal Eng.*, *31*, 163–198.

Davies, A. G., L. C. van Rijn, J. S. Damgaard, J. van de Graaff, and J. S. Ribberink (2002), Intercomparison of research and practical sand transport models, *Coastal Eng.*, *46*, 1–23.

Downing, A., P. D. Thorne, and C. E. Vincent (1995), Backscattering from a suspension in the near field of a piston transducer, *J. Acoust. Soc. Am.*, *97*, 1614–1620.

Emery, W. J., and R. E. Thompson (1997), *Data Analysis Methods in Physical Oceanography*, Elsevier, Amsterdam, Netherlands.

Faraci, C., and E. Foti (2002), Geometry, migration, and evolution of small-scale bed forms generated by regular and irregular waves, *Coastal Eng.*, *47*, 35–52.

Goring, D. G., and V. I. Nikora (2002), Despiking acoustic Doppler velocimeter data, *J. Hydraul. Eng.*, *128*, 117–126.

Grant, W. D., and O. S. Madsen (1982), Movable bed roughness in unsteady oscillatory flow, *J. Geophys. Res.*, *87*, 469–481, doi:10.1029/JC087iC01p00469.

Hanes, D. M., V. Alymov, Y. S. Chang, and C. Jette (2001), Wave-formed sand ripples at Duck, North Carolina, *J. Geophys. Res.*, *106*, 22,575–22,592, doi:10.1029/2000JC000337.

Hansen, E. A., J. Fredsoe, and R. Deigaard (1994), Distribution of suspended sediment over wave-generated ripples, *J. Waterw. Port Coastal Ocean Eng.*, *120*, 37–55.

Lee, T. H., and D. M. Hanes (1995), Direct inversion method to measure the concentration profile of suspended particles using backscattered sound, *J. Geophys. Res.*, *100*, 2649–2657, doi:10.1029/94JC03068.

Malarkey, J., and A. G. Davies (2002), Discrete vortex modeling of oscillatory flow over ripples, *Appl. Ocean Res.*, *24*, 127–145.

Malarkey, J., and A. G. Davies (2004), An eddy viscosity formulation for oscillatory flow over vortex ripples, *J. Geophys. Res.*, *109*, C12016, doi:10.1029/2003JC002086.

Marsh, S. W., C. E. Vincent, and P. D. Osborne (1999), Bed forms in a laboratory wave flume: An evaluation of predictive models for bed form wavelengths, *J. Coastal Res.*, *15*, 624–634.

Miller, M. C., and P. D. Komar (1980), Oscillation sand ripples generated by laboratory apparatus, *J. Sediment. Petrol.*, *50*, 173–182.

Moate, B. D., and P. D. Thorne (2009), Measurements and inversion of acoustic scattering from suspensions having broad size distributions, *J. Acoust. Soc. Am.*, *126*, 2905–2917.

Mogridge, G. R., M. H. Davies, and D. H. Willis (1994), Geometry prediction for wave-generated bed forms, *Coastal Eng.*, *22*, 255–286.

Nakato, T., F. A. Locher, J. R. Glover, and J. F. Kennedy (1977), Wave entrainment of sediment from rippled beds, *J. Waterw. Port Coastal Ocean Eng.*, *103*, 83–99.

Nichols, C. S., and D. L. Foster (2007), Full-scale observations of wave-induced vortex generation over a rippled bed, *J. Geophys. Res.*, *112*, C10015, doi:10.1029/2006JC003841.

Nielsen, P. (1983), Entrainment and distribution of different sand sizes under water waves, *J. Sediment. Petrol.*, *53*, 423–428.
Nielsen, P. (1986), Suspended sediment concentrations under waves, *Coastal Eng.*, *10*, 23–31.
Nielsen, P. (1992), *Coastal Bottom Boundary Layers and Sediment Transport*, World Sci., Sydney, Aust.
Osborne, P. D., and C. E. Vincent (1996), Vertical and horizontal structure is suspended sand concentrations and wave-induced fluxes over bed forms, *Mar. Geol.*, *131*, 195–208.
Pedocchi, F., and M. H. Garcia (2009), Ripple morphology under oscillatory flow: 1. Prediction, *J. Geophys. Res.*, *114*, C12014, doi:10.1029/2009JC005354.
Podgorski, K., I. Rychlik, and U. E. B. Machado (2000), Exact distributions for apparent waves in irregular seas, *Ocean Eng.*, *27*, 979–1016.
Sleath, J. F. A. (1984), *Sea Bed Mechanics*, John Wiley, New York, USA.
Sleath, J. F. A., and S. Wallbridge (2002), Pickup from rippled beds in oscillatory flow, *J. Waterw. Port Coastal Ocean Eng.*, *128*, 228–237.
Soulsby, R. L. (1997), *Dynamics of Marine Sands. A Manual for Practical Applications*, HR Wallingford, Wallingford, U.K.
Soulsby, R. L., and R. J. S. Whitehouse (2005), *Prediction of Ripple Properties in Shelf Seas*, HR Wallingford, Wallingford, U.K.
Styles, R., and S. M. Glenn (2002), Modeling bottom roughness in the presence of wave-generated ripples, *J. Geophys. Res.*, *107*(C8), 3110, doi:10.1029/2001JC000864.
Thorne, P. D., and D. M. Hanes (2002), A review of acoustic measurement of small-scale sediment processes, *Cont. Shelf Res.*, *22*, 603–632.
Thorne, P. D., and R. Meral (2008), Formulations for the scattering properties of suspended sandy sediments for use in the application of acoustics to sediment transport processes, *Cont. Shelf Res.*, *28*(2), 309–317.
Thorne, P. D., P. J. Hardcastle, and R. L. Soulsby (1993), Analysis of acoustic measurements of suspended sediments, *J. Geophys. Res.*, *98*, 899–910.
Thorne, P. D., J. J. Williams, and A. G. Davies (2002), Suspended sediments under waves measured in a large-scale flume facility, *J. Geophys. Res.*, *107*(C8), 3178, doi:10.1029/2001JC000988.
Thorne, P. D., A. G. Davies, and J. J. Williams (2003), Measurements of near-bed intrawave sediment entrainment above vortex ripples, *Geophys. Res. Lett.*, *30*(20), 2028, doi:10.1029/2003GL018427.
Thorne, P. D., A. G. Davies, and P. S. Bell (2009a), Observations and analysis of sediment diffusivity profiles over sandy rippled beds under waves, *J. Geophys. Res.*, *114*, C02023, doi:10.1029/2008JC004944.
Thorne, P. D., D. Hurther, B. D. Moate, R. D. Cooke, and F. X. Chassagne (2009b), Acoustic measurements of boundary layer flux profiles over a sandy rippled bed under regular waves, *Proc. Int. Conf. Underwater Acoust. Meas.*, *2009*, 517–524.
Tomkins, M. R., P. Nielsen, and M. G. Hughes (2003), Selective entrainment of sediment graded by size and density under waves, *J. Sediment. Res.*, *73*, 906–911.
Traykovski, P., A. E. Hay, J. D. Irish, and J. F. Lynch (1999), Geometry, migration, and evolution of wave orbital ripples at LEO-15, *J. Geophys. Res.*, *104*, 1505–1524, doi:10.1029/1998JC900026.
Tunstall, E. B., and D. L. Inman (1975), Vortex generation by oscillatory flow over rippled surfaces, *J. Geophys. Res.*, *80*, 3475–3484, doi:10.1029/JC080i024p03475.
van der Werf, J. J., J. S. Doucette, T. O'Donoghue, and J. S. Ribberink (2007), Detailed measurements of velocities and suspended sand concentrations over full-scale ripples in regular oscillatory flow, *J. Geophys. Res.*, *112*, F02012, doi:10.1029/2006JF000614.
van Rijn, L. C. (2007), Unified view of sediment transport by currents and waves, III: Graded beds, *J. Hydraul. Eng.*, *133*, 761–775.
Villard, P. V., and P. D. Osborne (2002), Visualization of wave-induced suspension patterns over two-dimensional bed forms, *Sedimentology*, *49*, 363–378.
Vincent, C. E. (2007), Measuring suspended sand concentrations using acoustic backscatter: A critical look at errors and uncertainties, in *Coastal and Shelf Sediment Transport*, edited by P. S. Balson and M. B. Collins, pp. 7–15, Geol. Soc. Publ. House, Bath, U.K.
Vincent, C. E., and D. M. Hanes (2002), The accumulation and decay of near-bed suspended sand concentration due to waves and wave groups, *Cont. Shelf Res.*, *22*, 1987–2000.
Wiberg, P. L., and C. K. Harris (1994), Ripple geometry in wave-dominated environments, *J. Geophys. Res.*, *99*, 775–789, doi:10.1029/93JC02726.
Wiberg, P. L., and C. R. Sherwood (2008), Calculating wave-generated bottom orbital velocities from surface-wave parameters, *Comput. Geosci.*, *34*, 1243–1262.
Williams, J. J., and P. S. Bell (2006), Laboratory investigation of bed form dynamics and resuspension of sandy sediments at field scale, *J. Coastal Res.*, *2*, 810–815.
Williams, J. J., P. S. Bell, L. E. Coates, N. Metje, and R. Selwyn (2003), Interactions between a benthic tripod and waves on a sandy bed, *Cont. Shelf Res.*, *23*, 355–375.
Williams, J. J., P. S. Bell, P. D. Thorne, N. Metje, and L. E. Coates (2004), Measurement and prediction of wave-generated suborbital ripples, *J. Geophys. Res.*, *109*, C02004, doi:10.1029/2003JC001882.
Williams, J. J., P. S. Bell, and P. D. Thorne (2005), Unifying large and small wave-generated ripples, *J. Geophys. Res.*, *110*, C02008, doi:10.1029/2004JC002513.

D. M. Hodgson and R. B. O'Hara Murray, School of Environmental Sciences, University of Liverpool, 4 Brownlow Street, Liverpool GB-L69 3GP, UK. (roryohm@liv.ac.uk)

P. D. Thorne, National Oceanography Centre, Joseph Proudman Building, 6 Brownlow Street, Liverpool GB-L3 5DA, UK.